Published in final edited form as:

Nature. 2023 September ; 621(7977): 206–214. doi:10.1038/s41586-023-06470-1.

A pentameric TRPV3 channel with a dilated pore

Shifra Lansky[1], **John Michael Betancourt**[1,2], **Jingying Zhang**[3,4,5], **Yining Jiang**[1,6], **Elizabeth D Kim**[1], **Navid Paknejad**[7,8], **Crina M Nimigean**[1,9], **Peng Yuan**[3,4,5], **Simon Scheuring**[1,9,*]

[1]Department of Anesthesiology, Weill Cornell Medicine, New York, NY, USA.

[2]Neuroscience Graduate Program, Graduate School of Medical Sciences, Weill Cornell Medicine, New York, NY, USA

[3]Department of Cell Biology and Physiology, Washington University School of Medicine, Saint Louis, MO, USA.

[4]Center for the Investigation of Membrane Excitability Diseases, Washington University School of Medicine, Saint Louis, MO, USA.

[5]Department of Pharmacological Sciences, Icahn School of Medicine at Mount Sinai, New York, NY, USA.

[6]Biochemistry & Structural Biology, Cell & Developmental Biology, and Molecular Biology (BCMB) Program, Graduate School of Medical Sciences, Weill Cornell Medicine, New York, NY, USA.

[7]Structural Biology Program, Memorial Sloan Kettering Cancer Center, New York, NY, USA.

[8]Physiology, Biophysics and Systems Biology Graduate Program, Weill Cornell Medical College, New York, NY, USA.

[9]Department of Physiology and Biophysics, Weill Cornell Medicine, New York, NY, USA

Abstract

Transient receptor potential (TRP) channels are a large, eukaryotic ion channel superfamily that control diverse physiological functions, and therefore are attractive drug targets.[1–5] More than 210 structures from over 20 different TRP channels have been determined, all are tetramers.[4] Despite this wealth of structures, many aspects concerning TRPV channels remain poorly understood, including the pore-dilation phenomenon, whereby prolonged activation leads to increased conductance, permeability to large ions, and loss of rectification.[6,7] Here, we used HS-AFM to analyze membrane-embedded TRPV3 at the single-molecule level and discovered a pentameric state. HS-AFM dynamic imaging revealed transience and reversibility of the pentamer

*Correspondence to: sis2019@med.cornell.edu.

Author contributions:

S.L and S.S designed the study; J.Z. and P.Y. expressed and purified protein from *P. pastoris* cells; S.L., J.M.B and E.D.K expressed and purified protein from *HEK GnTI*⁻ cells; S.L. and J.M.B reconstituted protein; S.L. performed negative stain EM imaging; S.L., E.D.K. and C.M.N. performed and analyzed electrophysiology measurements; S.L. and J.M.B performed HS-AFM imaging; S.L. and Y.J. performed HS-AFM data analysis; S.L. and J.M.B performed nanoDSF experiments and analysis; S.L. and J.M.B performed cryo-EM sample preparation and data collection; S.L., E.D.K and N.P. analyzed single particle cryo-EM data; S.L. and S.S performed channel structure analysis; Y.J performed and analyzed oligomer simulation; S.L and S.S wrote the paper; all authors edited the manuscript; S.S. supervised the project.

Competing interests

There are no competing financial interests.

in dynamic equilibrium with the canonical tetramer through membrane diffusive protomer exchange. The pentamer population increased upon diphenylboronic anhydride (DPBA) addition, an agonist that has been shown to induce TRPV3 pore-dilation. Based on these findings, we designed a protein production and data analysis pipeline that resulted in a cryo-EM structure of the TRPV3 pentamer, displaying an enlarged pore compared to the tetramer. The slow kinetics to enter and exit the pentameric state, the increased pentamer formation upon DPBA addition, and the enlarged pore, indicate that the pentamer represents the structural correlate of pore-dilation. We thus show membrane diffusive protomer exchange as an additional mechanism for structural changes and conformational variability. Overall, we provide first structural evidence for a non-canonical pentameric TRP-channel assembly, laying the foundation for new directions in TRP-channel research.

Transient receptor potential (TRP) channels form a large superfamily of ion channels that are widely expressed in eukaryotes such as vertebrates, invertebrates, yeast, and algae.[1,2] TRP-channels respond to multiple types of stimuli and are involved in a diverse range of biological processes including sensory functions such as thermosensation, nociception, and taste perception, as well as fluid secretion, ion homeostasis, and lysosomal, immune cell, cardiac, and smooth muscle functions.[3,4] As a result of their widespread expression and physiological roles, mutations in TRP-channels lead to many disorders and diseases such as pain, atopic dermatitis, asthma, cardiac disease, and neurological and metabolic disorders.[5] Significant progress in understanding TRP-channel structure and function was achieved with the first TRP-channel structure (TRPV1) determination by single-particle cryo-EM,[8] a feat that marked the beginning of membrane protein structure determination within the cryo-EM resolution revolution.[9] Since then more than 210 structures have been solved from over 20 different TRP-channels, all displaying a tetrameric assembly (Extended Data Figure 1).[4]

The TRPV family, named after the vanilloid ligand-binding site,[10] consists of the six proteins TRPV1–6. TRPV1–4 belong to the temperature-activated TRP-channels (thermo-TRPs),[11] while TRPV5–6 are calcium-selective channels involved in Ca^{2+}-uptake.[12] TRPV1–4, however, are not only activated by heat, but are also activated by various natural and synthetic ligands (*e.g.* TRPV1 (capsaicin),[10] TRPV2 (cannabidiol),[13] TRPV3 (carvacrol, camphor, thymol),[14] TRPV4 (anandamide, arachidonic acid)[15]). To date, more than 130 TRPV structures have been solved, in the absence and presence of ligands and in various conformational states, with several representative structures from each family member (Extended Data Figure 1, top).[4] The architectures of all TRPV-channels resemble each other, consisting primarily of a large intracellular ankyrin repeat domain (ARD), and a transmembrane domain (TMD) composed of six helices (S1-S6). Helices S1-S4 form a voltage sensor-like domain (VSLD) while S5-S6 form the pore domain (PD). TRPV-channels contain additionally a coupling domain (composed of a linker domain, the pre-S1 helix, and the C-terminal domain (CTD)), a selectivity filter (SF), and the conserved TRP helix at the interface of the lipid bilayer and the cytoplasm (Figure 1a,b).[8,16] These domains are arranged in a so-called domain-swapped organization so that helices S1-S4 of one subunit interact with helices S5-S6 of a neighboring subunit in the tetramer (Figure 1c).

However, despite the wealth of TRPV-channel structures, many details of the gating cycle remain unclear and disputed, *e.g.*, how does heat trigger activation, what are the structural correlates of the states along the functional cycle (including sensitized and desensitized states), and the role of the many ligand-binding sites in the ligand-activation mechanisms of TRPV-channels.[13,17–19] An additional structurally controversial issue concerns the pore-dilation phenomenon.[6,7] This phenomenon has functionally been reported for TRPV1,[20–24] TRPV3,[25] TRPA1,[26,27] and a TRPV2 mutant,[28] whereby prolonged activation by heat and/or agonists leads to a dramatic increase in conductance, loss of ion selectivity, permeability to large cations such as N-Methyl-D-glucamine ($NMDG^+$), Tris(hydroxymethyl)aminomethane ($Tris^+$) and 2-(methyl-amino)-ethanol ($2\text{-}MAE^+$), and loss of rectification, suggesting a dilation of the channel pore over time. While the canonical activation kinetics is fast, in the milliseconds range, pore dilation occurs on the seconds-to-minutes time scale.[7] The slowness of its occurrence implicates that it is separated by a large energy barrier from the canonical open state.[7] Thus, the pore-dilated state appears to be qualitatively different from the canonical activated state both structurally, with a markedly enlarged pore, and kinetically, being adopted at timescales that are unusually long for a typical protein conformational change.

To address some of these unresolved issues, we used here high-speed atomic force microscopy (HS-AFM)[29,30] to directly image in buffer solution and at physiological temperature and pressure membrane-embedded full-length human TRPV3 at the single-molecule level with a temporal resolution of ~1 second. We reasoned that to get insights into some of the remaining questions, a novel technique, so far not used to analyze TRP-channels, with qualitatively different abilities, could be beneficial. We reveal that TRPV3 channels can adopt a hitherto unobserved pentameric state, and that this pentameric state is rare, reversible, and transient, *i.e.*, the tetrameric state is interconvertible with the pentameric state on the seconds-to-minutes timescale through membrane diffusive exchange of protomers. We additionally demonstrate that the prevalence of the pentameric state is increased 2-fold upon addition of diphenylboronic anhydride (DPBA), a synthetic agonist that has been shown to lead to enhanced TRPV3 currents associated with pore-dilation.[25] Armed with the knowledge about this noncanonical state and how it was reached, we adapted protein production and analysis workflows allowing us to determine the cryo-EM structure of the TRPV3 pentamer to 4.4 Å resolution, revealing a wide channel pore, substantially larger than the pores in tetramers. Overall, our results show that TRPV3 channels can adopt a pentameric state that may be the structural correlate to the functionally pore-dilated state and may pave the way for a new avenue in TRP-channel research.

Pentameric TRPV3 channels in membranes

To directly image human TRPV3 by HS-AFM, we reconstituted purified channels (expressed either in *P. pastoris* or in HEK293S cells, Methods, Supplementary Figure 1) into liposomes at a lipid-to-protein ratio (LPR) between 0.5 and 2.5, using either yeast polar lipids or a mixture of POPC (1-palmitoyl-2-oleoyl-glycero-3-phosphocholine), DOPS (1,2-dioleoyl-sn-glycero-3-phospho-L-serine) and cholesterol at a ratio of 8:1:1 (w:w:w) (Methods). The reconstitution process (Supplementary Figure 2) and the resulting proteo-liposomes (Figure 1d) were observed using negative-stain EM. We confirmed

the functionality of the TRPV3 channels in the reconstitutions by single-channel electrophysiology recordings (Extended Data Figure 2). For HS-AFM analysis, the proteo-liposomes were deposited on freshly cleaved mica and imaged in buffer solution, revealing membrane patches of ~150 nm in size containing densely packed tetrameric TRPV3 channels (Figure 1e, Supplementary Videos 1–4). Height distribution (Figure 1f) and cross-section (Figure 1g) analyses from such overview HS-AFM images demonstrated that the channels had an overall thickness of ~8.5 nm and protruded from the membrane by ~4 nm, indicating that the channels exposed the large ARD domains at the intracellular face of the protein to the HS-AFM tip.

However, surprisingly, upon close inspection of the HS-AFM videos, we detected pentameric TRPV3 alongside the canonical tetrameric channels (Figure 2a, arrowheads, Supplementary Videos 5–9). We acquired high-magnification HS-AFM scans to resolve the pentamers together with their tetrameric neighbors at high resolution (Figure 2b, Supplementary Videos 10–14). To computationally corroborate the stoichiometry of the two molecular species, we plotted radial profiles of the particles, which allowed us to discriminate particles with 5 peaks in the radial profile with ~72° periodicity from particles with 4 peaks in the radial profile with ~90° periodicity (Figure 2c). Next, we calculated correlation averages of the tetramer and pentamer channels (Figure 2d, insets) from particles in the same HS-AFM frames (Figure 2b, panel 2), thus recorded under identical loading force and relative tip-sample velocity. These averages corroborated the increased size and a larger central cavity of the pentamer channel as compared to the tetramer. Section profiles, where the tetramer was analyzed along a straight line (Figure 2d, green line in top inset), while the pentamer was analyzed along a line with a 144° inclusion angle (Figure 2d, purple line in bottom inset), revealed quantitatively that the protomers in both oligomeric states had similar topography, but the pentamer was larger (Figure 2d, grey arrowheads) and the tip could enter deeper into the central pore (Figure 2d, black arrowhead), certainly due to the geometrical rearrangement of the subunits. Finally, we analyzed the protrusion height of tetramer and pentamer over the lipid bilayer (Figure 2e, left, Figure 2b, panel 4), plotting the height values in histograms (Figure 2e, middle and right) and as a function of time (Supplementary Figure 3). Gaussian fitting of the resulting height distributions indicated that the tetramer and pentamer had indistinguishable protrusion height, $\Delta h_{\text{tetramer}} = 4.7$ nm (FWHM = 0.5 nm) (Figure 2e, middle) and $\Delta h_{\text{pentamer}} = 4.7$ nm (FWHM = 0.5 nm) (Figure 2e, right), respectively, in excellent agreement with the height of the intracellular ARD domain in the cryo-EM tetramer structure (see Figure 1c, bottom). Thus, HS-AFM structure and topography characteristics of the protomers in the tetramer and pentamer were identical within error. Along with the fact that we analyzed purified and reconstituted protein, all data indicated that the tetramer and pentamer channels indeed are different oligomeric states of the same TRPV3 subunits.

Yet, the strongest evidence that the tetrameric and pentameric TRPV3 channels are indeed built from the same subunits, that the two oligomeric species represent relevant states of the same protein, and that the subunits retain a native-like fold in both states, would be the direct observation of their ability to interconvert. To show this, we needed to acquire well-resolved HS-AFM videos over extended periods of time (minutes), longer than the typical lifetime of the pentameric state, at a temporal resolution that oversamples the lifetimes of the

states. Thus, we acquired HS-AFM videos (Supplementary Videos 15–21) at 0.5 s temporal resolution over durations from ~3 to ~20 minutes. In such HS-AFM videos, we found direct evidence that the pentameric state was transient and reversible. We observed canonical tetrameric TRPV3 channels that transitioned into pentamers (Figure 3a,b, Extended Data Figure 3a–f, Supplementary Videos 15–17), pentamers that transitioned into tetramers (Figure 3c,d, Extended Data Figure 3g–k, Supplementary Videos 18–20), and complete tetramer–pentamer–tetramer (Figure 3e, Extended Data Figure 3l, Supplementary Video 21) and pentamer–tetramer–pentamer (Figure 3f, Extended Data Figure 3m) transitions. Monitoring complete events was extremely challenging as they are rare and many of them likely occurred on timescales that exceed our typical HS-AFM video acquisition duration. In total, we observed 29 unambiguous transition events (Figure 3g). From the pentamer–tetramer transition observations, we calculated a rough estimate of 192 s (Figure 3h), and from the duration of 65 pentamer observations without transition we estimated a lower bound of 172 s (Figure 3i), of the typical lifetime of the pentameric state (Methods). Occasionally, the resolution of our videos was high enough to resolve the individual subunit that ‘attacked’ and inserted into a tetramer (Figure 3b, Extended Data Figure 3c,e,m) or dissociated from a pentameric TRPV3 channel (Figure 3d,f, Extended Data Figure 3h,j,k,m). Logically, the interchange of the oligomeric state must be accompanied by the existence of free TRPV3 subunits in the membrane. Indeed, we observed the dissociation of tetramers into trimers, dimers, and monomers, and additionally, in rare cases, we observed various fragments assembling into tetrameric channels (Extended Data Figure 4). Thus, tetrameric and pentameric channels are composed of the same TRPV3 subunits that dynamically interchange through 2D membrane diffusion. The subunit exchange and diffusion limitation of the process provide the characteristics of slowness to insert and form a pentamer and dissociate from a pentamer, and thus the high energy barrier to enter and exit the noncanonical pentameric TRPV3 channel state.

The HS-AFM topography revealed a substantially enlarged cavity at the pore entrance on the intracellular surface of the pentamer as compared to the tetramer (Figure 2b,d), which we attributed to a geometric enlargement of the pore upon the insertion of a fifth subunit. Indeed, if one were to use simply geometric considerations to evaluate the incircle diameter (D), incircle area (A_D), and polygon area (A), of a pentagon and a square with equal side lengths $a_{(5)} = a_{(4)}$, one receives, $D_{(5)} = 1.38 \bullet D_{(4)}$, $A_{D(5)} = 1.89 \bullet A_{D(4)}$, and $A_{(5)} = 1.72 \bullet A_{(4)}$. Such an increase in pore size would suggest that the pentameric state should have a much-increased conductance, permeability to larger ions, and loss of selectivity and rectification, similar to the properties reported for the pore-dilated state.[6,7,25] Additionally, our state transition analysis demonstrated that the pentamer state was entered through two rather slow processes, protomer 2D membrane diffusion and insertion into tetramers, and exited after ~3 minutes lifetime through a reverse process, corresponding well to the seconds-to-minutes timescale previously reported necessary to enter and exit the pore-dilated state.[21,25]

DPBA increases pentamer population

To investigate whether the TRPV3 pentamer with its slow kinetics and enlarged pore might relate to previous functional descriptions of pore dilation, we imaged TRPV3 by HS-AFM in presence of 320 μM diphenylboronic anhydride (DPBA), a ligand that has previously

been shown to induce pore-dilation in TRPV3.[25] In prior studies, 320 μM DPBA led to enhanced TRPV3 currents and loss of ion selectivity and rectification associated with pore dilation.[25] HS-AFM imaging of TRPV3 in the presence of this activator revealed the coexistence of tetramers, pentamers, and fragments in the membrane (Figure 4a, Supplementary Videos 22–25), similar to the situation in the absence of DPBA (see Figures 1,2). At the resolution of HS-AFM, no apparent structural differences could be detected between DPBA-activated and apo-TRPV3 (Figure 4a). While we did not quantitatively assign the fragments to specific oligomeric states, some of the fragments were rather clearly resolved as monomers, dimers, and trimers (Figure 4a, grey arrowheads and associated numbers) along with tetramers and the pentamers (Figure 4a, white arrowheads). Counting the TRPV3 tetramers, pentamers, and fragments in our HS-AFM videos (Methods) revealed that the percentage of pentamers and fragments significantly increased in the presence of DPBA, while the percentage of tetramers decreased (Figure 4b). Specifically, when taking into account only the tetramer and pentamer molecules, the pentamer population increased from 10.5 ± 1.2 % to 18.4 ± 0.3 % upon DPBA addition; while, when also taking fragments (≤ 3 protomers) into account, the pentamer population increased from 11.6 ± 1.3% to 18.2 ± 0.5%, and the fragment population from 9.1 ± 0.5 % to 17.1 ± 1.0 %, while the tetramer population decreased from 79.3 ± 1.0% to 64.7 ± 0.5% (Figure 4b, Supplementary Tables 1–2). These results indicated that DPBA addition destabilized TRPV3 tetramers, and the increased abundance of freely diffusing protomers in the membrane favored the formation of noncanonical assemblies and the emergence of TRPV3 pentamers.

To further investigate the destabilizing effect of DPBA on the TRPV3 tetrameric state, we performed nano differential scanning fluorimetry (NanoDSF)[31,32] experiments and measured the thermal stability of TRPV3 by monitoring changes in the 350/330 nm fluorescence emission as a function of temperature. In NanoDSF experiments, the intrinsic fluorescence of the protein's tryptophanes (Trp) and tyrosines (Tyr) is measured, which change in response to alterations in their local environment during, for example, temperature-dependent conformational changes, oligomer dissociation and/or unfolding. Interestingly, the thermal denaturation profiles of TRPV3 revealed two first derivative peaks corresponding to two melting temperatures, the first melting temperature (Tm1) reported by a reverse blueshift profile with an inflection point at 55.5 ± 0.1 °C and the second melting temperature (Tm2) with an inflection point at 63.4 ± 0.3 °C (Figure 4c,d). Notably, when adding to the same protein sample 320 μM DPBA, Tm1 decreased to 52.7 ± 0.6 °C and Tm2 decreased to 61.3 ± 0.5 °C. When adding instead 32 μM and 100 μM DPBA, ligand concentrations that have been shown to induce canonical activation but not the secondary enhanced current,[25] the melting temperatures were closer to the apo condition, *i.e.*, 55.1 ± 0.5 °C and 54.5 ± 0.3 °C for Tm1 and 63.1 ± 0.3 °C and 62.6 ± 0.6 °C for Tm2, respectively (Figure 4c,d). Finally, when adding to the sample 1000 μM DPBA, a ligand concentration that has been shown to lead to breakdown of the conductance, an even more dramatic decrease in stability is observed, 51.3 ± 1.0 °C and 60.5 ± 0.3 °C for Tm1 and Tm2, respectively (Figure 4c,d). A redshift in the 350/330 nm fluorescence signifies exposure of buried Trp residues, whereas a blueshift in the fluorescence correlates to the absence of buried Trp residues or the exposure of buried Tyr residues upon thermal denaturation.[31,32] Examining the distribution of Tyr and Trp in the TRPV3 structure, we

found many buried Trp and Tyr residues, and specifically, many Tyr buried at the interfaces between subunits (Supplementary Figure 4). This led us to suggest that Tm1 corresponds to a breakup of the TRPV3 oligomer manifested by exposure of buried Tyr residues at the subunit interfaces, while Tm2 corresponds to denaturation of the TRPV3 protomer. An alternative interpretation would be that Tm1 relates to temperature-sensing conformational changes and Tm2 to protomer breakage and denaturation altogether. Whatever the detailed sequence of events, DPBA clearly impacts the integrity of the protomer interfaces and destabilizes the channel. Thus, these results are in line with the decrease of tetramers and the increase of TRPV3 fragments that we observed by HS-AFM following DPBA addition.

Cryo-EM structure of the TRPV3 pentamer

Knowing that pentamer formation critically depended on 2D membrane diffusive protomer exchange, and encouraged by the observation that addition of DPBA increased the occurrence of pentamer molecules in the membrane, we set out to determine a cryo-EM structure of the pentamer using an adapted protein production pipeline: First, while the channels were still in the membrane, before extraction, we exposed them to 320 μM DPBA and 2 mM camphor (since camphor has been shown to synergize with DPBA for TRPV3 activation)[33]. We hypothesized that exposure to activators while still in the membrane would allow an increased fraction of channels to reach the pentameric state through protomer exchange before they were isolated into single particles. Second, during size exclusion chromatography (SEC) purification, we decided not to select the highly homogenous SEC peak but rather chose the left shoulder of the SEC peak (Supplementary Figure 1c) prone to contain larger sized particles. After flash-freezing this fraction onto grids, 10,118 cryo-EM micrographs were collected (Extended Data Table 1), revealing many tetrameric molecules that produced through single-particle analysis straightforwardly a 2.6 Å resolution map of the canonical tetrameric TRPV3 (Figure 5a, Extended Data Figures 5,6a,c). Notably, amongst the tetrameric molecules, we could also detect in the raw data a small percentage of channels (in top view) with clear pentameric architecture (Figure 5b,c). Using enhanced particle picking and classification processes to parse out this pentameric state (Extended Data Figure 5, Methods), we identified 8% pentameric particles in various orientations (Figure 5d). These pentameric particles were then further classified into a more homogenous pentamer stack (2% of total particles), leading to reconstruction of a 4.4 Å resolution map of a channel comprising five subunits with clear TRP-channel architecture, arranged in a domain-swapped fashion (Figure 5e, Extended Data Figure 6b).

Despite the relatively low resolution of this map (the TMD regions are of lower resolution, ~5.0–5.5 Å, than the cytoplasmic domains (Extended Data Figure 6b)), some sidechain densities could be identified, allowing the modeling of a pentameric structure into this map, where 39% of sidechain positions could be assigned (Extended Data Figure 6d, Methods). Analysis of the TRPV3 pentamer structure confirms that, similarly to the TRPV3 tetramer (Figure 5a, Extended Data Figure 7a), each TRPV3 pentamer subunit contains four transmembrane helices S1-S4 composing the VSLD, two transmembrane helices S5-S6 composing the PD, a SF, a TRP helix, and a large ARD intracellular domain (Figure 5e, Extended Data Figure 6,7b). However, certain regions of the pentamer map were unclear and disordered such as the coupling domain (composed of the linker domain, pre-S1

helix, and CTD), which was modeled with less confidence using constraints from the tetramer structure; or missing, such as the S4-S5 linker and the various loops connecting the TMD helices. Superposition of a TRPV3 pentamer subunit onto a TRPV3 tetramer subunit (aligned on the PD) reveals that the ARD, VSLD, and TRP helix in the pentamer subunit are rotated by ~18° with respect to the tetramer subunit, opening up a wider space between the PD and VSLD (Extended Data Figure 7c,d). Such a rotation allows the neighbor subunit to interact at a 108° angle instead of a 90° angle as in the tetramer, and therefore accommodates insertion of a fifth subunit into the channel. This hinge-like rearrangement within each subunit allows the domain-swap interactions between subunits to be largely preserved. Namely, the interactions between helix S5 of one subunit with helices S1 and S4 of a neighboring subunit (PD-VSLD interaction), and the S6-S6 and SF-SF interactions (PD-PD interaction) between neighboring subunits, are generally maintained (Extended Data Figure 7e). The buried surface area (BSA) between two subunits is 5,426 $Å^2$ in the tetramer compared to only 1,014 $Å^2$ in the pentamer (Extended Data Figure 7f–g). Although the pentamer BSA is likely an underestimate given the incompleteness of the pentamer model, a smaller BSA between subunits in the pentamer correlates well with the lesser stability of the pentameric state, as apparent from its low population percentage and short lifetime.

Structural superposition of our TRPV3 tetramer structure onto the structure of a previously published closed conformation TRPV3 structure (PDB 6UW4),[16] reveals almost no structural deviation (root mean square deviation (RMSD) of 1.05Å; Supplementary Figure 5), indicating our tetramer structure was also captured in a closed conformation. Indeed, when comparing the pore profiles of our tetramer structure *vs.* the open conformation structure of a TRPV3 mutant (K169A; PDB 6UW6)[16], a significantly narrower constriction is observed at the SF and gate regions (Figure 5f,g), corroborating that we obtained a closed conformation. Notably, when comparing the pore profile of the TRPV3 pentamer *vs.* the pore profiles of the tetramers (taking into consideration only the backbones, since not all sidechains were resolved in the pentamer structure), a large widening of the pore could be observed, with diameters of 8.4 Å at the SF and 13.4 Å at the gate, as compared to 1.2 Å (SF) and 5.8 Å (gate) for the closed tetramer, and 3.5 Å (SF) and 8.4 Å (gate) for the open tetramer structure (Figure 5h; Supplementary Table 3). Thus, the diameter of the SF and gate in the pentamer increases 7.0-fold (SF) and 2.3-fold (gate), respectively, when compared to the tetramer closed conformation, and 2.4-fold (SF) and 1.6-fold (gate), respectively, when compared to the tetramer open conformation. Furthermore, when comparing the average diameter of the backbone pore (calculated using all radii values between SF and gate), the pentamer pore is 1.8-fold and 1.5-fold enlarged when compared to the tetramer closed and open conformations, respectively (Supplementary Table 3). Of course, the most important value is the 2.4-fold diameter increase between pentamer (8.4 Å) and open state tetramer (3.5 Å) at the selectivity filter, *i.e.*, at the narrowest constriction. This significantly enlarged pore in the TRPV3 pentamer strengthens our hypothesis that the TRPV3 pentamer has a much-increased conductance, permeability to larger ions, and loss of selectivity and rectification, similarly to the pore-dilated state in TRP-channels.

Here, we reveal that TRPV3 can adopt a pentameric state with an enlarged pore. To the best of our knowledge, this is the first alternative oligomeric state for any TRP-channel, and for any channel of the large tetrameric cation channel family with the helix - pore-loop - helix

fold in general.[34] Using HS-AFM, we demonstrate tetramer-to-pentamer and pentamer-to-tetramer transitions, even the reversibility of the pentameric TRPV3 state, and place the stability of the TRPV3 pentamer in the ~3 minutes lifetime range. Using single-particle cryo-EM, we determined the structure of the TRPV3 pentamer, revealing a wide-open channel pore, 2.4-fold larger than the open state tetramer at the SF constriction.

The reversibility and transience of the TRPV3 pentamer, and the fact that the transient character of the state depends on membrane diffusion of protomers, makes the TRPV3 pentamer qualitatively different from other activated states. Typically, states can be induced through the addition of ligands, or other biochemical or physical cues, and thus can be reproduced in vitro and/or on a cryo-EM grid. This is not the case for the TRPV3 pentamer. Once a tetrameric channel is extracted from the membrane and in a detergent micelle or nanodisc, it cannot convert into the pentameric state, even upon the addition of the in-principle-correct agent. In addition, typical structural biology experiments are performed on protein samples that are purified to excellent homogeneity (SEC elution peak), data acquisition and processing further select for most abundant species (in 3D-crystals, or through particle selection in single-particle cryo-EM), and the averaging processes in structure determination diminish the ability to determine rare and transient states, providing explanations why the TRPV3 pentamer has so far eluded discovery by cryo-EM and other averaging-based structural methods. HS-AFM, with nanometer lateral and sub-second temporal resolution of single molecules provides unique possibilities to discover and describe rare, short-lived transient states.

As surprising as is the occurrence of such a pentameric state, the slow membrane diffusion process that is involved in this change (as compared to a canonical conformational change), fit well the seconds-to-minutes timescale that has been reported to reach a pore-dilated state in functional experiments.[7] This is the first finding that links the pentamer to pore-dilation. We then tested whether pore-dilation agent DPBA addition favored pentamer formation,[25] and found a ~2-fold increase in TRPV3 pentamers and destabilization of tetramers. This is the second finding that tightens the pentamer to pore-dilation. Finally, taking advantage of our knowledge from HS-AFM experiments that the pentameric state was reached through 2D membrane diffusion and that DPBA addition increased the pentamer population, we rationalized cryo-EM experiments that allowed us to solve a structure of the pentameric state (Methods). The TRPV3 pentamer structure displays a ~7.0-fold and ~2.4-fold enlarged pore at the SF compared to the tetramer closed and open conformations, respectively, constituting the third finding that correlates the pentamer to the pore-dilated state.

In TRPV1, pore-dilation is induced upon addition of the activator capsaicin or lysophosphatidic acid (LPA).[21,23,24] LPA led to increased unitary channel currents and whole-cell conductance.[23] Prolonged activation by capsaicin led to an increase in pore diameter, which allowed permeation of large cations such as 2-MAE$^+$, Tris$^+$, and NMDG$^+$.[21] The structure of TRPV1 with capsaicin has been solved,[35] where the activator binds in the vanilloid binding pocket shared among all TRPVs, which is located at the VSLD – PD domain-swap interface (Supplementary Figure 6a). Thus, it is imaginable that activators, or LPA, fragilize inter-protomer contacts and favor dissociation of tetramers. In this context, in TRPV6 a single mutation at the VSLD – PD interface led to a non-swapped tetrameric

TRPV6.[36] Clearly, the VSLD – PD interface is a sensitive region. We thus propose that pore-dilation agents (*e.g.*, capsaicin or LPA in TRPV1, 2-APB, DPBA in TRPV3, and temperature) destabilize inter-protomer interactions, especially the domain-swap VSLD – PD interface. In TRPV3 no structure with bound DPBA has been determined, but structures with 2-aminoethoxydiphenyl borate (2-APB), a synthetic agonist that is structurally-related to DPBA, are available.[37] Although 2-APB has not been shown to bind to the vanilloid pocket but to several different sites located in the VSLDs and the ARD-TMD linker[16,38,39] (Supplementary Figure 6b), binding of DPBA (assuming DPBA binds to TRPV3 similarly to 2-APB) might allosterically destabilize inter-protomer interactions. This speculation is supported by our finding that DPBA, at a concentration shown to induce pore-dilation, reduced the melting temperature of TRPV3 (Figure 4c,d), *i.e.*, destabilized the protein by some yet unknown mechanism. Finally, it is noteworthy that gain-of function mutations in genetic diseases are not located in the pore but rather at the VSLD – PD inter-protomer interfaces.[40,41]

Our HS-AFM data provide direct visual evidence that TRPV3 monomers ‘attack’ and insert into tetramers to form pentamers, and that the reverse transition occurs through dissociation of a monomer from the pentamer to form a tetramer rather than through full pentamer disassembly (Figure 3b,d,f, Extended Data Figure 3c,e,h,j,k,m). We also provide direct evidence that all states are reversible, *i.e.*, tetramers can dissociate into trimers, dimers, and monomers, and that various fragments can assemble back to form a tetramer (Extended Data Figure 4). Taken together, we propose the following model for the formation of TRPV3 pentamers (Extended Data Figure 8): Canonical tetrameric TRPV3 are activated by natural and/or pore-dilation agents, which are typically hydrophobic and intercalate the helices in the vanilloid pocket or at proximal sites. As a result, inter-protomer interactions are destabilized and tetramers may dissociate into trimers, dimers, and monomers. Monomers can then either assemble with other fragments to reform tetramers, or, alternatively, ‘attack’ another tetramer to form a pentamer. After seconds-to-minutes, pentamers shed a subunit to regain the tetrameric state. Protomer dissociation and insertion from and to tetramers and pentamers must be associated with flow of lipids, where lipids dynamically occupy and vacate space in the membrane and at protein interfaces during protomer exchanges.

Equilibrium distributions of 9:1 (HS-AFM) or 49:1 (cryo-EM) give free energy difference terms between the tetramer and pentamer of ~2.3k_BT or ~3.9k_BT, respectively. Such a free energy difference should be accessible through physiological changes. We hypothesize that there is a high energy barrier between the states, such as to extract and insert protomers, and to lipidate and delipidate them, respectively, during the processes. This energy barrier might be modulated by hydrophobic activators, or through environmental changes such as lipids. For example, lipids of varying thickness alone can influence membrane protein and subunit interactions by several k_BT.[42] Experiments with tetramer- or pentamer-concatemers could provide further insights into the functional characteristics and accessibility of canonical activated and pore-dilated states.[43]

Interestingly, the ability of cells to enter the secondary high-conduction, non-rectified state was favored in cells with increased TRPV3 abundance.[25] This finding is well explained by our model: Since the encounter probability of membrane diffusive protomers with tetramers

is crucial for pentamer formation, an increased protein density (2D-concentration) directly impacts formation of pore-dilated pentamers. Our model also explains why at very high DPBA concentrations (>1 mM), a breakdown of conductance was detected.[25] Accordingly, a compound that, at low concentration induces dissociation of some tetramers to give rise to monomers and the subsequent formation of strongly conducting pentamers, will, upon excessive addition drive the equilibrium towards the monomeric non-conductive state. Indeed, 1 mM DPBA significantly decreased the stability of TRPV3 (Figure 4c,d).

To assess our model further, we simulated the time evolution of tetramers and pentamers with a minimal number of parameters, *i.e.*, the stability of the different oligomers, and that monomers can associate with dimers, trimers, and tetramers to form new oligomeric states (Methods). The simulation reached after ~500 simulation steps a stable equilibrium population of 85% tetramers, ~15% pentamers, and a background of lower oligomers, where the pentamers had a ~4-fold shorter lifetime than the tetramers (Extended Data Figure 9). Thus, with a minimal set of parameters, simulation reproduced similar equilibrium populations and stabilities as observed experimentally.

Finally, our findings indicate a conceptually novel mechanism for membrane protein conformational changes: 2D membrane diffusion. Classically, we think of conformational changes as processes that take place within proteins. In contrast, here, we show a conformational change that occurs through a change in the oligomeric state via 2D membrane diffusive exchange of protomers. This concept should stimulate new avenues of membrane research that considers the subunit exchange as a possible way to modulate function and that accesses unusually long timescales. For example, $GABA_A$ receptors are known to exist in an impressive variety of heteromeric complexes.[44,45] In the context of TRPV channels, a report provided evidence of TRPV1-TRPV3 heteromeric channels.[46] One could hypothesize that heteromeric channels could form through membrane diffusive protomer exchange, similar to the mechanism we report to reach the TRPV3 pentameric state.

To summarize, we discovered here, using HS-AFM, a pentameric state of a TRP-channel. The TRPV3 pentamer is a rare and transient state that is in a reversible equilibrium with the canonical tetramer, and its formation is membrane diffusion dependent. An agent that was formerly documented to induce pore-dilation increased pentamer abundance by ~2-fold in our experimental setup. We also solved, using cryo-EM, a structure of the pentameric TRPV3 channel and found that it had a ~2.4-fold increased pore diameter at the SF compared to the canonical open state, and should therefore be highly conductive, nonselective, and allow passage of larger ions. Other characteristics are the slowness of the pentamer formation and dissociation processes through subunit diffusive exchange that make the TRPV3 pentamer a good candidate for the structural correlate to what has been described as the pore-dilation phenomenon. A pentameric pore-dilated TRPV channel state that would allow influx of large ions and Ca^{2+} should have major physiological impact in TRPV channel related diseases,[40,41] and possibly also in the regulation of other Ca^{2+}-sensitive biological processes.[47–49] Much more research is required to confirm our hypotheses, but our findings, presented here, lay the foundation for a new avenue in TRP-channel research.

Methods

TRPV3 purification from P. pastoris

The full-length human TRPV3 channel was expressed and purified as previously.[16] Briefly, the human TRPV3 DNA (GenBank: EAW90503.1) was inserted into the pPICZ-B vector, which contains a C-terminal PreScission protease cleavage site and a GFP-His_{10} tag, and transformed into *P. pastoris*. Yeast cells expressing human TRPV3 were cultured at 30°C, and protein expression was induced at 24°C. Cells were disrupted by milling (Retsch MM400) and resuspended in lysis buffer containing 50 mM Tris-HCl pH 8.0, 150 mM NaCl, protease inhibitors (2.5 μg/ml leupeptin, 1 μg/ml pepstatin A, 3 μg/ml aprotinin, 1 mM benzamidine, 100 μg/ml 4-(2-Aminoethyl) benzenesulfonyl fluoride hydrochloride, and 200 μM phenylmethane sulphonylfluoride), and DNase I. Cell membranes were solubilized with 1% lauryl maltose neopentyl glycol (LMNG, Anatrace) at 4°C for 2h and centrifuged at 30,000g for 30 min. The supernatant was mixed with 3 ml cobalt-charged resin (G-Biosciences) by rotating at 4°C for 3h. The resin was then washed with 30 ml wash buffer (20 mM Tris-HCl pH 8.0, 150 mM NaCl, 10 mM imidazole and 85 μM glyco-diosgenin (GDN, Anatrace)). After removing the GFP-His_{10} tag by using PreScission protease overnight at 4°C, the protein sample was collected and injected into Superose 6 Increase 10/300 gel filtration column (GE Healthcare Life Sciences) pre-equilibrated with buffer containing 20 mM Tris-HCl pH 8.0, 150 mM NaCl and 40 μM GDN. Peak fractions were collected and concentrated to ~5 mg/ml (Supplementary Figure 1a).

TRPV3 purification from HEK cells

The full-length human TRPV3 DNA was cloned into a pEGBacMam vector[50], with a C-terminal thrombin cleavage site followed by a streptavidin affinity tag. Bacmid growth and isolation were carried out according to the manufacturer protocol, using DH10Bac competent cells (Bac-to-Bac, Invitrogen). Three generations of baculovirus were made in Sf9 cells (ATCC, catalog no. CRL-1711) using established protocols[50], and the final generation (P3), used subsequently for transfection of HEK293S GnTI^{-} cells (ATCC, catalog no. CRL-3022), was concentrated x10 prior transfection (ultracentrifugation at 28,000 rpm (Ti45 Beckman rotor) for 1 h followed by resuspension in Gibco FreeStyle 293 media supplemented with 2% heat-inactivated fetal bovine serum (FBS)). 800 ml of HEK293S GnTI^{-} cell suspension, grown in FreeStyle 293 media with 2% FBS at 37 °C, 5% CO_2, were transfected with 1% concentrated P3 baculovirus, and 24 h post-transduction, 10 mM sodium butyrate was added to the suspension for a continued 48 h of expression at 30 °C. These cells were then pelleted and resuspended in lysis buffer containing 20 mM Tris, pH 8, 150 mM NaCl a protease inhibitor cocktail (Halt™ Protease Inhibitor Cocktail (Thermo Scientific)), and 1mM β-mercaptoethanol (βME). Cells were sonicated with a Q500 sonicator (QSonica), and then centrifuged for 15 min at 5000 g. The supernatant was subjected to ultracentrifugation at 40,000 rpm (Ti45 Beckman rotor), and the pelleted membranes were solubilized for 2 h in buffer containing 2% (wt/vol) digitonin with constant stirring at 4°C. For cryo-EM structure determination, the pelleted membranes were resuspended in buffer containing 320 μM DPBA and 2 mM camphor, with constant stirring for 15 min at 4°C, prior to addition of 2% digitonin. The solubilized membranes were then centrifuged for 0.5 h at 20,000 rpm, and the supernatant was added to 25 mL of Strep-Tactin

Sepharose resin (iba) with rotation overnight at 4 °C. Resin was washed with 50 mL of Wash Buffer (20 mM Tris-HCl pH 8.0, 150 mM NaCl, 1 mM βME, and 0.01% (w/v) glyco-diosgenin (GDN)) and eluted with 30 ml of the same buffer supplemented with 2.5 mM D-desthiobiotin. The elution fraction was then concentrated and further purified on a Superose 6 column (GE Healthcare Life Sciences) using the Wash Buffer (Supplementary Figure 1b,c). For cryo-EM structure determination, the shoulder fraction (Supplementary Figure 1c) was concentrated to ~2.5 mg/ml.

Proof of cell line authentication was provided by the vendor (ATCC). In addition, we examined the morphology of the cells and observed the successful outcome of the experiments (*i.e.*, successful virus generation with the sf9 cells and successful TRPV3 expression with the HEK293S GnTI- cells, using the HEK293S GnTI- cell dedicated plasmid pEGBacMam vector. Cell lines were tested negative for Mycoplasma contamination every few months throughout the research project. HEK293S GnTI- cells were used in this study since TRPV3 expresses very well in these cells.

TRPV3 reconstitution

Yeast Polar lipids or a lipid mixture consisting of POPC (1-palmitoyl-2-oleoyl-glycero-3-phosphocholine), DOPS (1,2-dioleoyl-sn-glycero-3-phospho-L-serine), and cholesterol at a ratio of 8:1:1 (w:w:w) (Avanti Polar Lipids) were solubilized with 1% glyco-diosgenin (GDN) detergent to a final lipid concentration of 4 or 8 mg/ml, respectively. These lipid mixtures were then mixed with purified TRPV3 (expressed either in *p. pastoris* or HEK293S GnTI^{-} cells) to final protein concentrations of 0.6 – 1.3 mg/ml, at a lipid-to-protein ratios (LPR) between 0.5 and 2.5 (w:w). After equilibration for 4–12 hr at 4 °C, detergent was removed by biobeads over the course of 3–4 days (Supplementary Figure 2). Successful formation of reconstituted vesicles was monitored with negative-stain electron microscopy (EM) using a 100 kV JEOL JEM1400 and a Veleta 2K x 2K TEM CCD camera (iTEM version 1.4.104 software, Olympus-Soft Imaging Solutions).

TRPV3 electrophysiology

Single channel recordings of TRPV3 in planar lipid bilayers were performed in a horizontal lipid bilayer setup at room temperature in 20 mM Tris-HCl, pH 8, 150 mM NaCl, 3 mM $CaCl_2$ buffer, in the presence and absence of diphenylborinic anhydride (100 μM DPBA, Sigma). Cis and trans chambers were separated by a 1,2-diphytanoyl-sn-glycero-3-phosphocoline (8 mg/ml DPhPC, Avanti Polar Lipids) bilayer solubilized in n-decane painted over a 100 μm diameter hole partition. TRPV3 proteo-liposomes, reconstituted in Yeast Polar lipids (Avanti Polar Lipids) at lipid-to-protein ratios (LPR) between 5 and 20 (w:w), were applied to the cis chamber. Currents were recorded in gap-free mode in Clampex 10.7.0.3 (Molecular Devices) using an Axopatch 200B amplifier (Molecular Devices) with a gain of 20, filtered online at 2 kHz and digitized at 20 kHz (Digidata 1440A, Molecular Devices). Currents were further filtered offline at 0.5–1kHz (as indicated) with an eight-pole, low-pass Bessel filter and the open probabilities and single-channel current amplitudes over a range of voltages were analyzed with the single-channel detection mode in Clampfit 10.7.0.3 (Molecular Devices).

High-speed atomic force microscopy

A 2 μL drop of TRPV3 reconstituted vesicles was deposited on a 1.5 mm^2 freshly cleaved mica surface, which was glued with UV glue to a quartz sample stage. After 5 minutes incubation in a humid chamber, the sample on the stage was gently rinsed with imaging buffer (20 mM Tris-HCl, pH 8.0, 150 mM NaCl for ligand-free (apo) conditions; 20 mM Tris-HCl, pH 8.0, 150 mM NaCl, and 320 μM Diphenylborinic anhydride (DPBA) for pore dilation conditions) and mounted in the HS-AFM fluid cell. In the presence of 150mM NaCl, a thin buffer layer (~5Å) separates the supported membrane from the mica support allowing membrane proteins to diffuse,[42] as reported here by the lateral and rotational motions of the TRPV3 channels in the densely packed membranes. Images were taken at room temperature with a HS-AFM (SS-NEX, RIBM, Japan), operated in amplitude modulation mode with optimized scan and feedback parameters, using the IgorPro RIBM software (Ibis 1.1.0, IgorPro 6.3.7.2). Ultrashort (8 μm) cantilevers (USC-F1.2-k0.15, NanoWorld, Switzerland) with a nominal spring constant of 0.15 N/m, a resonance frequency of~650 kHz and a quality factor of ~1.5 in buffer, were used. Igor Pro version 8 (WaveMetrics, USA) was used for HS-AFM data collection. Oxygen plasma etching was used to sharpen the tips. HS-AFM images were taken at 0.5 to 3 frames per second at pixel-sampling ratios of 1.25 to 8 Å/px. HS-AFM imaging under very similar conditions has allowed to analyze the structure and dynamics of several other membrane proteins, such as OmpG, AqpZ, ec-CLC, GltPh, CorA, Piezo-1, GLIC,[42,51–57] and never were changes in oligomerization observed as are documented here for TRPV3. HS-AFM video alignment, flattening, and cross-section, height distribution, and radial profile analyses were carried out in ImageJ (version 1.53h, Java 1.8)[58,52]

Oligomer population analysis

Tetramers, pentamers, and fragments (≤ 3 protomers) were counted by eye from 109 HS-AFM videos of unique membrane patches in apo condition, and from 99 HS-AFM videos imaged in presence of 320 μM DPBA. Percentage of pentamers was calculated either relative to the number of tetramers and pentamers combined (Figure 4b, left) or relative to the total number of protomers observed (with fragments considered as 2 protomers on average) (Figure 4b, right), calculated as the mean values (+/− SEM) of percentages derived from n=3 biologically independent samples. Statistical significance was assessed with the one-tailed two proportion Z-test, yielding in all cases p-values < 0.0001.

Pentamer lifetime analysis

To obtain an estimate for the typical lifetime of the pentamer state, we plotted the dwell times of the pentamer states that were observed to transform into tetramers, specifically, the pentamer observations that had an end but no beginning (n=11), and the complete pentamer observations had both a beginning and an end (n=6) (Figure 3g). Assuming a Markov model for the pentamer – tetramer transition, we fitted the resulting histogram (Figure 3h) with an exponential decay $e^{-\beta t}$ (adj. R^2=0.77) and obtained an estimate of $\beta = 0.0052\ s^{-1}$ and $\tau = 1/\beta = 192$ s for the typical lifetime of the pentamer. We plotted additionally the dwell times (Figure 3i) for our “stable” pentamer observations, *i.e.*, the pentamer observations that had no beginning nor end (Figure 3g), and obtained a mean dwell time of $< \tau > = 172$ s. Since

the stable pentamer observations have yet to transition into tetramers, the mean dwell time of these observations should provide a lower limit to the typical pentamer lifetime, which is notably shorter than the estimate of 192 s we obtained from the Markov model. Additionally, if we were to calculate the mean dwell time of our complete pentamer observations (n=6), we received $<\tau>$ = 190s. All estimates point towards a characteristic pentamer lifetime of ~3 minutes.

Nano differential scanning fluorimetry

NanoDSF thermal denaturation curves were measured for purified TRPV3 expressed in HEK293S GnTI$^-$ cells, using the peak fraction from the SEC column corresponding to a pure tetramer, diluted to 3.3 μM concentration (in 20 mM Tris-HCl pH 8.0, 150 mM NaCl, 1 mM βME, and 0.01% (w/v) GDN). Measurements were conducted in apo conditions and upon addition of 32 (n=6 biologically independent experiments), 100 (n=6), 320 (n=7), and 1000 μM (n=6) DPBA, using a Tycho NT.6 (NanoTemperTech) machine according to the manufactor's instructions. Statistical significance was assessed with the one-tailed unequal variance (Welch's) T-test, yielding a significant reduction (99% confidence level) in both Tm1 and Tm2 following addition of 320 μM DPBA (p-value=0.000038 and 0.00190, respectively), and a further reduction in Tm1 and Tm2 following addition of 1000 μM DPBA (p-value=0.015 (95% confidence) and 0.0043 (99% confidence).

Cryo-EM sample and data collection

TRPV3, purified from HEK293S GnTI$^-$ cells and subjected to 320 μM DPBA and 2mM camphor while still in membrane, before solubilization (see section "TRPV3 purification from HEK293S GnTI- cells"), was used for cryo-EM structure determination. 3.5 μl of this preparation, from the left shoulder fraction of the SEC concentrated to ~2.5 mg/ml (Supplementary Figure 1b,c), was deposited onto glow-discharged Quantifoil R1.2/1.3, 400 mesh, copper grids. A FEI Vitrobot Mark IV automated EM grid plunge freezer was used to blot the grids (blot time 2 s, blot force 3, wait time 20 s, 100% humidity, 4 °C) and plunge-freeze them into liquid ethane. TRPV3 data were collected from two such grids using an EF-Krios electron microscope at the New York Structural Biology Center (NYSBC), operated at 300 kV, with a GatanK3 imaging system collected at 64,000x nominal magnification, in super-resolution mode (0.538 Å/pixel) and subsequently binned to the physical pixel size of 1.076 Å/pixel for processing. Videos were collected using Leginon version 3.6[59] at an exposure rate of 26.6 $e^-/Å^2/s$ with a total exposure of 2.0 s, for an accumulated electron exposure of 53.3 $e^-/Å^2$. Intermediate frames were recorded every 0.05 s for a total of 40 frames per micrograph. A total of 10,125 images were collected at a nominal defocus range of 0.8–2.5 μm under focus (Extended Data Table 1).

Cryo-EM image processing

All major data processing steps were conducted with cryoSPARC version 3.3.2,[60] unless otherwise stated, and are summarized in Extended Data Figure 5. Namely, drift and beam-induced motions were corrected using Patch Motion Correction, and the contrast transfer function (CTF) was estimated using Patch CTF Estimation. Blob Picking (diameter 100–200 Å) was used to pick an initial set of particles, extracted with a box size of 256 pixels, and then used for calculation of initial 2D class averages. The best 2D class

averages were used for a second round of particle picking using Template Picking, and the best 2D classes resulting from these picks were used for training and for a third round of particle picking using Topaz (version 0.2.4),[61] resulting in a total of 3,668,517 picked particles. 2D classification of these particles (150 classes) resulted in classes clearly corresponding to a tetrameric state (18 classes, 1,532,979 particles), and 6 classes bearing some resemblance to a pentameric state (237,786 particles; Extended Data Figure 5). The tetrameric classes were subjected to Ab-initio 3D reconstruction (C1 symmetry) and Homogenous Refinement (C4), resulting in a 2.6 Å resolution map, as estimated by the Fourier shell correlation (FSC) = 0.143 criterion calculated between two independent half maps,[62] and in a local resolution range of 2.4–4.5 Å (Extended Data Figure 6a,c), as computed by Local Resolution Estimation in cryoSPARC (version 3.3.2). In parallel, the 6 “somewhat pentameric” classes were subjected to Ab-initio 3D classification (5 classes; C1 symmetry), resulting in two 3D classes with 5-fold symmetry features. The particles contributing to these classes (84,676 particles) were subjected to another round of 2D classification (100 classes), resulting in 4 classes with clear 5-fold symmetry (3,935 particles). These particles were subjected to Ab-initio 3D reconstruction (C1), and after confirming a 5-fold symmetry of the resulting map, it was refined with Homogenous Refinement (C5 symmetry), resulting in an incomplete but clear pentameric map at 10.2 Å resolution (Extended Data Figure 5). Heterogenous Refinement was then performed (C1 symmetry), using the Topaz particle stack (3,668,517 particles) as input, and 8 reference maps corresponding to 3 duplicates of the initial pentamer map (10.2 Å), the tetramer map (2.6 Å), and 8 decoy noise maps, generated as described previously.[63] This calculation resulted in 12 3D classes, corresponding to 3 pentamer, 1 tetramer, and 8 noise maps. The particles contributing to the pentamer and tetramer classes were then submitted for another round of Heterogenous Refinement, and the reference pentamer map previously used was updated to an improved and more complete map generated by subjecting the pentamer classes (obtained through Heterogenous Refinement) to Ab-initio classification (C1) and Homogenous and Non-Uniform Refinement (C5). This selection process was repeated iteratively 18 times, until it converged to 1,525,490 tetramer particles (similarly to the number obtained earlier for tetrameric particles) and 133,788 pentamer particles. This pentamer stack produced a 7.8 Å resolution map after Ab-initio classification (C1) and Homogenous Refinement (C5). To further improve this map, the pentamer particles were subjected to 5 rounds of Ab-initio 3D classification (3 classes, C1 symmetry) to further remove junk particles, whereby the particles corresponding to the best class were used as input for the next round of Ab-initio classification. After each classification cycle, maps were calculated from each class to check that the resolution indeed improved. This process converged finally to a map at 4.9 Å (using Homogenous and Non-uniform refinement (C5 symmetry), corresponding to 41,737 clear pentamer particles (Figure 5d). These particles were then subjected to Bayesian polishing with Relion 4.0,[64] after which the particles for which polishing was not correctly applied were removed through 3 rounds of Heterogenous Refinement cycles, similarly to the procedure described above. These cycles converged on 30,186 polished pentamer particles, which after Homogenous and Non-Uniform refinement, resulted in a 4.4 Å resolution map (FSC = 0.143 criterion), and in a local resolution range of 4.1–7.0Å (Extended Data Figure 6b) as computed by Local Resolution Estimation in cryoSPARC (version 3.3.2). Finally, this map was subjected to density modification using

Resolve CryoEM in PHENIX (version 1.20.1–4487),[65] leading to a significantly improved map, where some sidechain densities could clearly be observed (Extended Data Figure 6d). Calculating the pentamer map without imposed symmetry (C1) resulted in less clear maps and lower reported FSC resolution than for maps calculated in C5. Therefore, we concluded that the pentameric state has no statistical deviation from 5-fold symmetry but has rather high intrinsic flexibility or is under internal stress, in agreement with the reduced stability of the pentameric state.

Cryo-EM structure model building

To build the TRPV3 tetramer, the cryo-EM structure of human TRPV3 previously published (PDB 6UW4)[16] was used as a starting model to dock into the map with Chimera (version 1.13.1).[66] 34 lipid molecules were modeled into lipid-like densities, using the lipids present in the mouse TRPV3 structure (PDB 7MIJ, 1.98 Å)[17] as reference initial structures. Refinement of the model into the map was conducted by iterative rounds of real space refinement with PHENIX (version 1.20.1–4487)[67] followed by manual adjustment in Coot (version 0.9.8.1).[68] Model validation was performed with MolProbity,[69] providing good geometrical parameters (Extended Data Table 1). To build the TRPV3 pentamer, a monomer from the 6UW4 tetramer structure, truncated to poly-alanine, was docked five times into the density-modified pentamer map using Chimera (version 1.13.1),[66] and then relaxed and refined further into the map using real space refinement in PHENIX (version 1.20.1–4487)[70] (with secondary structure, reference model, and NCS restraints). Then, using Coot (version 0.9.8.1),[68] certain sidechains were modeled into regions with clear sidechain densities, which determined the placement of the rest of the sequence into the map under the general secondary structure restraints of the tetramer structure. Once the pentamer model position was determined with good confidence, additional sidechains were added to the model (for a total of 39% of the modeled sequence), while in regions with no clear densities sidechains were truncated. To maintain good geometry, MolProbity (version 4.2)[69] was used for geometrical validation, and iterative cycles of real space refinement in PHENIX (version 1.20.1–4487)[70] (with progressively relaxed constraints) and manual adjustments in Coot (version 0.9.8.1)[68] were performed until good geometrical parameters were achieved (Extended Data Table 1). Structure analysis was conducted with Pymol (version 2.3.3), Chimera (version 1.13.1) and VMD (version 1.9.4).

Oligomer lifetime simulation

We built with Matlab (version R2021b) a simple model to simulate the interchange of tetramers to pentamers (and lower oligomeric states) based on a minimal set of parameters (Extended Data Figure 9). Based on the experimental pentamer lifetime analysis (Figure 3g,h), the less favorable protomer interaction interface angle of 108° *vs.* 90° (Extended Data Figure 7c,d), the ~10 times lesser abundance (Figure 4b), and the lesser BSA (Extended Data Figure 7f,g), of the pentamer as compared to the canonical tetramer, we associated lesser stability to the pentamer than to the tetramer. Because in trimers and dimers protomers make only one neighbor contact, while all protomers make two contacts with neighbors in tetramer and pentamer, the stability of low oligomeric states, <4, was set weaker. The simulation was built on the Markov chain Monte Carlo method (MCMC) with 6 states: empty, monomer, dimer, trimer, tetramer, and pentamer. We denote m_k as a general

expression for the states, where $k = \{0,1,2,3,4,5\}$ stands for empty, monomer, dimer, trimer, tetramer, or pentamer, and E_1 to E_5 stands for the stability of states m_1 to m_5, respectively.

In each iteration (time) step t, the state is updated based on the equilibrium energies of the oligomer transitions and the probability of encountering a monomer, $P(t,\ m_1)$. We only allow transitions between adjacent states, thus Δk can only be 0 or 1. At each iteration (time) step, the probabilities from the current state m_k to all possible states at step $t+1$, $P(t+1, \ldots/t, m_k)$, are evaluated:

$$P(t+1, m_k|t, m_k) = 1/Z \quad \text{eq. 1}$$

$$P(t+1, m_{k+1}|t, m_k) = (1-\delta_{k,5})P(t,\ \ m_1)\exp(E_k - E_{k+1})/Z \quad \text{eq. 2}$$

$$P(t+1, m_{k-1}|t, m_k) = (1-\delta_{k,1})\exp(E_k - E_{k-1})/Z \quad \text{eq. 3}$$

where,

$$Z = 1 + (1-\delta_{k,5})P(t,\ \ m_1)\exp(E_k - E_{k+1}) + (1-\delta_{k,1})\exp(E_k - E_{k-1}) \quad \text{eq. 4}$$

is the partition function. The delta function $\delta_{a,b} = \begin{cases} 1, & a = b \\ 0, & a \neq b \end{cases}$ excludes impossible transitions. Here, eq. 1 characterizes the probability of having the same state at the next time step, eq. 2 characterizes the probability of an association event if the current state is not a pentamer, and eq. 3 characterizes the probability of a dissociation event if the current the state is not a monomer.

The simulation has S parallel trails (spaces) and T total time steps. At each time step t, the probability of encountering a monomer is calculated according to the updated count of monomers, $N(t,\ m_1)$, and empty spaces, $N(t, m_0)$, as $P(t,\ m_1) = \frac{N(t,\ m_1)}{N(t,m_1)+N(t,m_0)}$. In short, the state, m_k, at the next time step, $t+1$, is updated by picking a uniform random number $u \in [0,1]$, and comparing it with the transition probabilities, *i.e.* the accumulative sum of eq. 1, eq. 2 and eq. 3. A freshly formed monomer emerging from a dissociation event is moved to an empty space in the same time step.

The simulation presented with $S = 5250$ and $T = 2000$, was initialized at $t=1$ with 5000 spaces filled with the tetramer state (m_4) and 250 spaces assigned with the empty state (m_0). The stability of the states was characterized by state energies $E=\{E_1,E_2,E_3,E_4,E_5\}=\{4,4,4,-2,-1.8\}$. The condition with 5000 tetramers in a space of 5250 locations is set to mimick a densely packed membrane.

Data and code availability statements

All data and materials to draw the conclusions of this manuscript are presented in the main text, figures, and the extended data figures and supplementary videos. The cryo-EM maps

of the TRPV3 tetramer and pentamer have been deposited in the Electron Microscopy Data Bank with accession codes EMD-40181 and EMD-40183, respectively, and their structural models have been deposited in the Protein Data Bank with accession codes 8GKA and 8GKG, respectively (Extended Data Table 1). Further data can be received from the corresponding author upon reasonable requests.

Extended Data

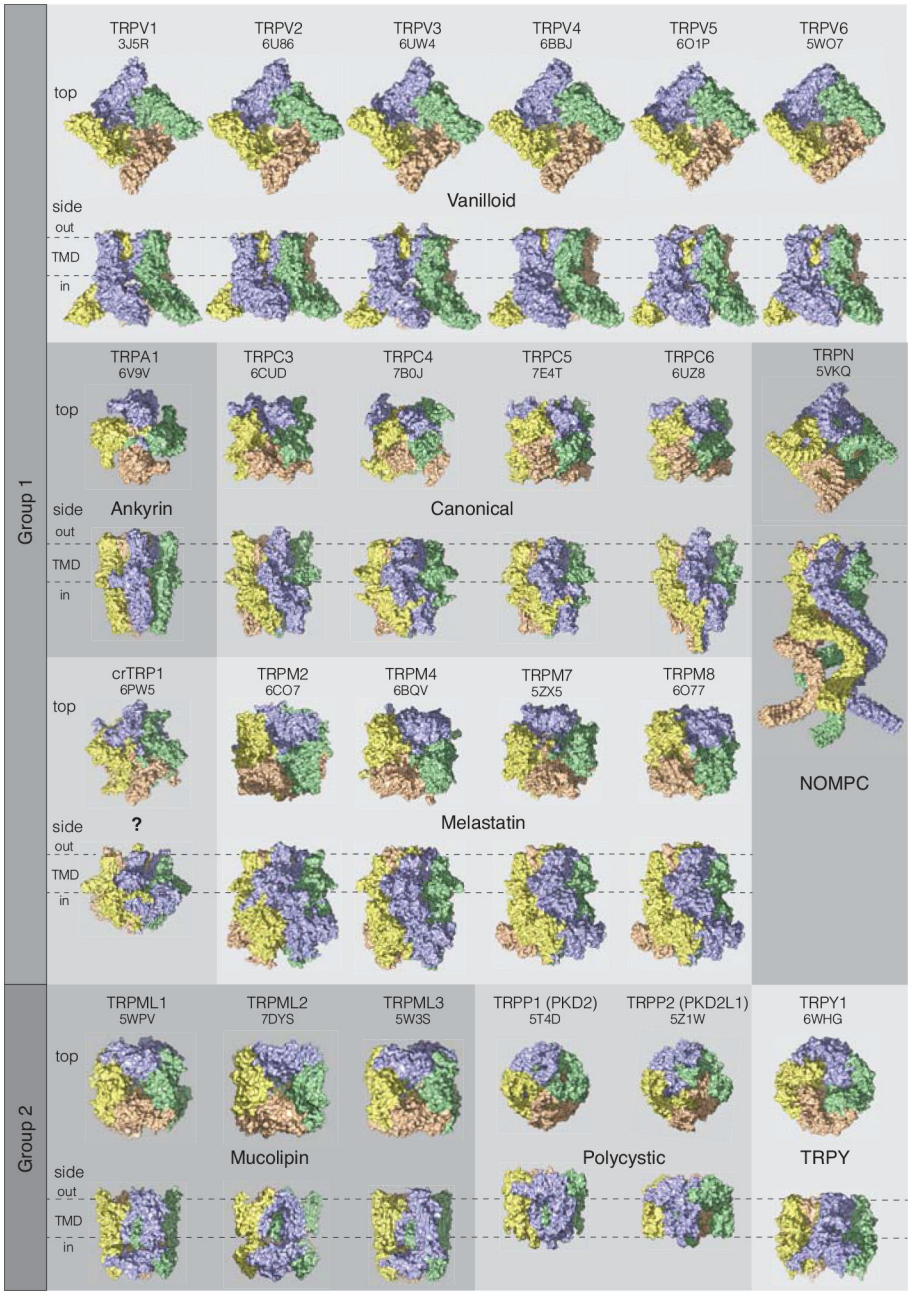

Extended Data Figure 1 |. TRP-channel structures.

Representative structures (out of >210 structures) of the 22 TRP-channels solved so far. All structures are tetramers, with the four subunits colored in wheat, green, purple and yellow. Each structure is depicted in surface representation, shown from the intracellular (top) and side (bottom) views. The question mark in the crTRP1 panel signifies that the subfamily to which crTRP1 belongs is yet unknown.

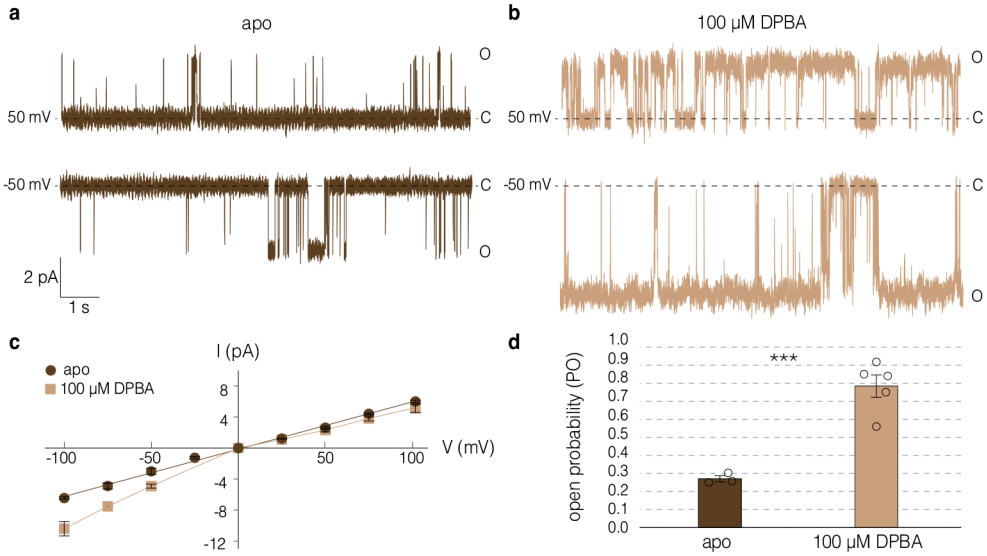

Extended Data Figure 2 |. Single-channel recordings of TRPV3.

(a) and **(b)** Representative single-channel recordings of TRPV3 in the absence (a) and presence (b) of 100 µM DPBA, at −50 and 50 mV. (**c**) Since-channel current-voltage (IV) curves of TRPV3 obtained from −100 to 100 mV, in the absence and presence of 100 µM DPBA. (**d**) Single-channel open probabilities determined from recordings obtained at −50 mV, in the absence and presence of 100 µM DPBA. Open probability values (0.27 ± 0.01 and 0.78 ± 0.05 respectively) were derived as the mean values +/− SEM from $n \geq 3$ independent experiments (circles). Statistical significance was assessed with the one-tailed Welch's T-test, yielding a significant (p-value = 0.0007) increase in open channel probability following DPBA addition. All recordings were performed on TRPV3 channels from one purification following the same protein expression and purification protocol as for the cryo-EM analysis and reconstituted following the same protocol as for the HS-AFM analysis though at higher lipid-to-protein ratio (LPR between 5 and 20 for electrophysiology recordings *vs.* LPR between 0.5 and 2.5 for HS-AFM experiments). *** p-value <0.005.

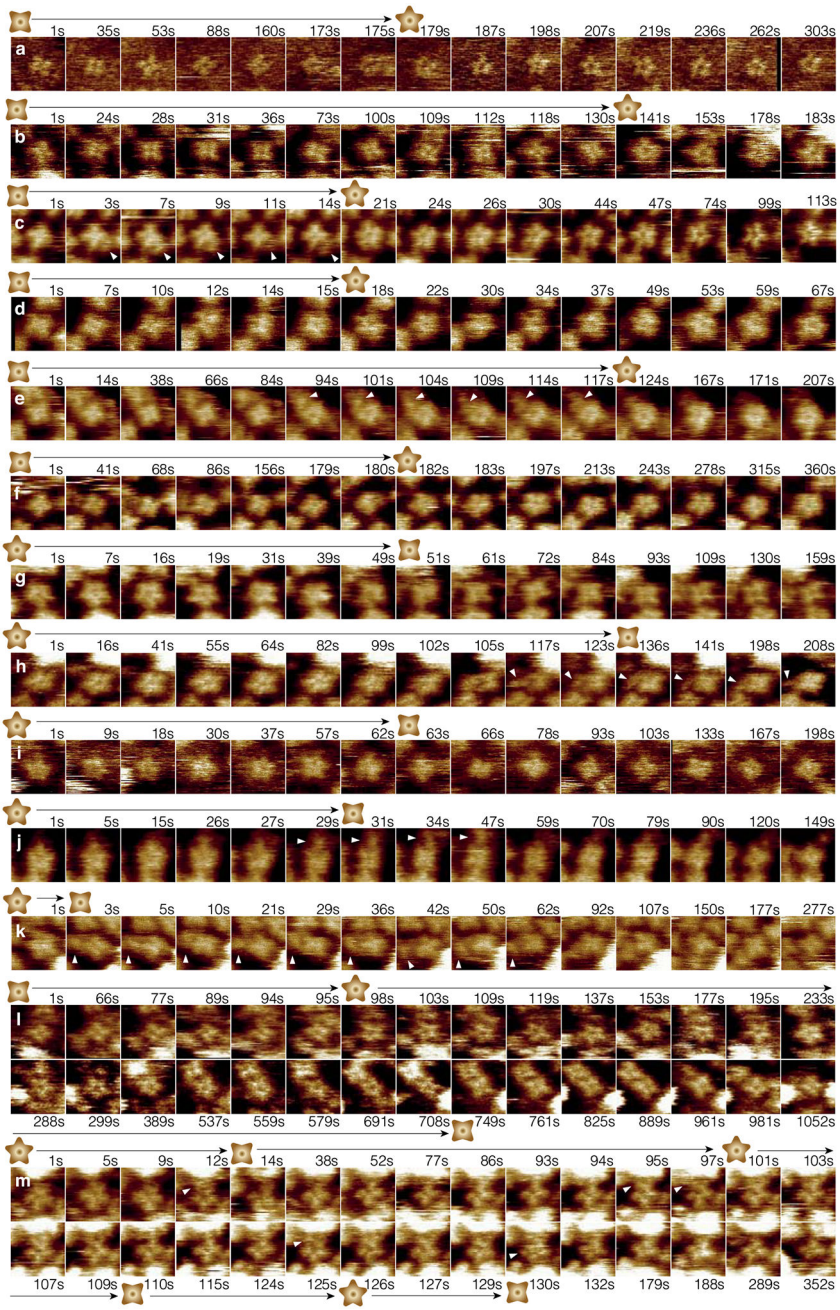

Extended Data Figure 3 |. The TRPV3 tetramer and pentamer are reversible.

(a) to **(f)** Tetramer to pentamer transitions. **(g)** to **(k)** Pentamer to tetramer transitions. **(l)** TRPV3 tetramer-pentamer-tetramer transition. **(m)** TRPV3 pentamer-tetramer-pentamer-tetramer-pentamer-tetramer transition. White arrowheads indicate the occasionally observed monomers ‘attacking’ and inserting into tetramers to yield pentamers, and the observed monomers dissociating from pentamers to yield tetramers.

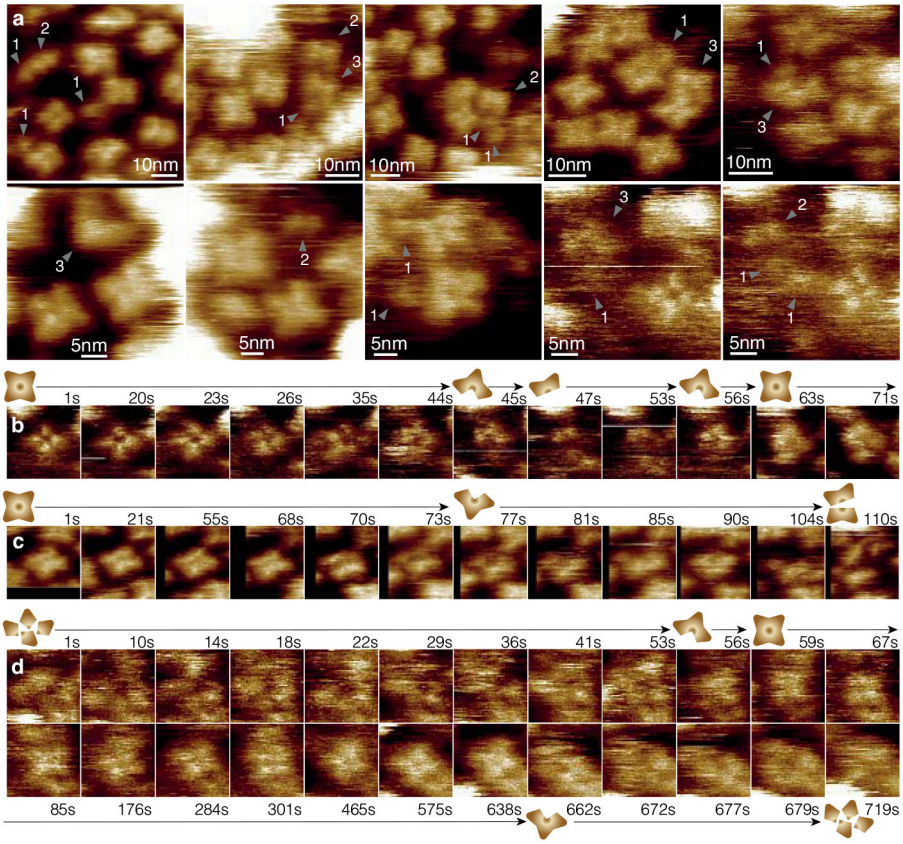

Extended Data Figure 4 |. TRPV3 tetramers can breakup into fragments and reform.

(a) TRPV3 tetramers and pentamers coexist alongside TRPV3 ≤ 3 protomer fragments. Grey arrowheads indicate monomer (1), dimer (2), and trimer (3) fragments. **(b)** and **(c)** TRPV3 tetramer breakups into trimer and dimer. **(d)** TRPV3 fragments form a stable tetramer, which then breaks apart.

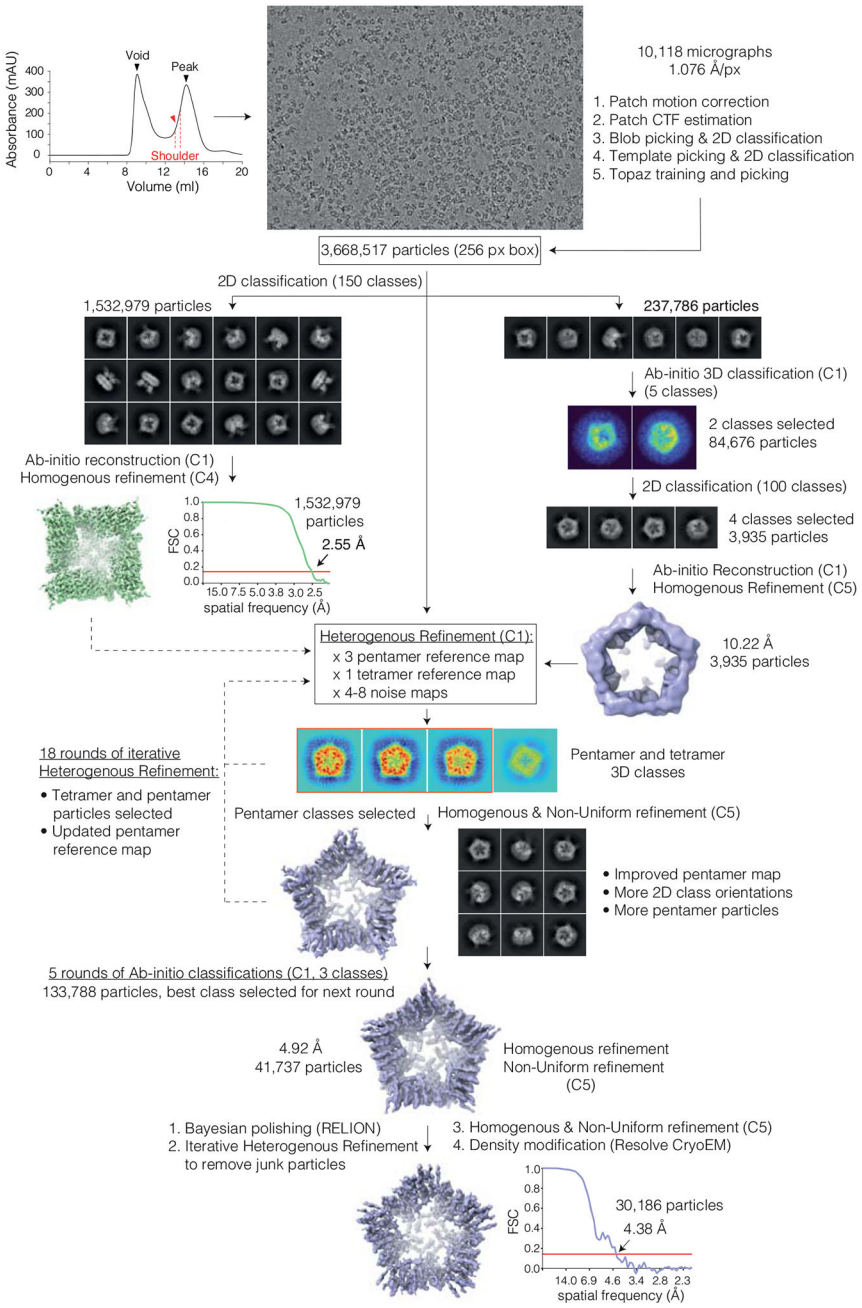

Extended Data Figure 5 |. Workflow for cryo-EM reconstruction of the TRPV3 tetramer and pentamer.

Flowchart for the cryo-EM data processing, particle picking, classification, and reconstruction, enabling map reconstruction of the tetramer at 2.55Å resolution and for the pentamer at 4.38Å resolution. Unless otherwise stated, all processing steps were conducted in cryoSPARC version 3.3.2. Dashed lines indicate the inputs used for the iterative cycles of heterogenous refinement.

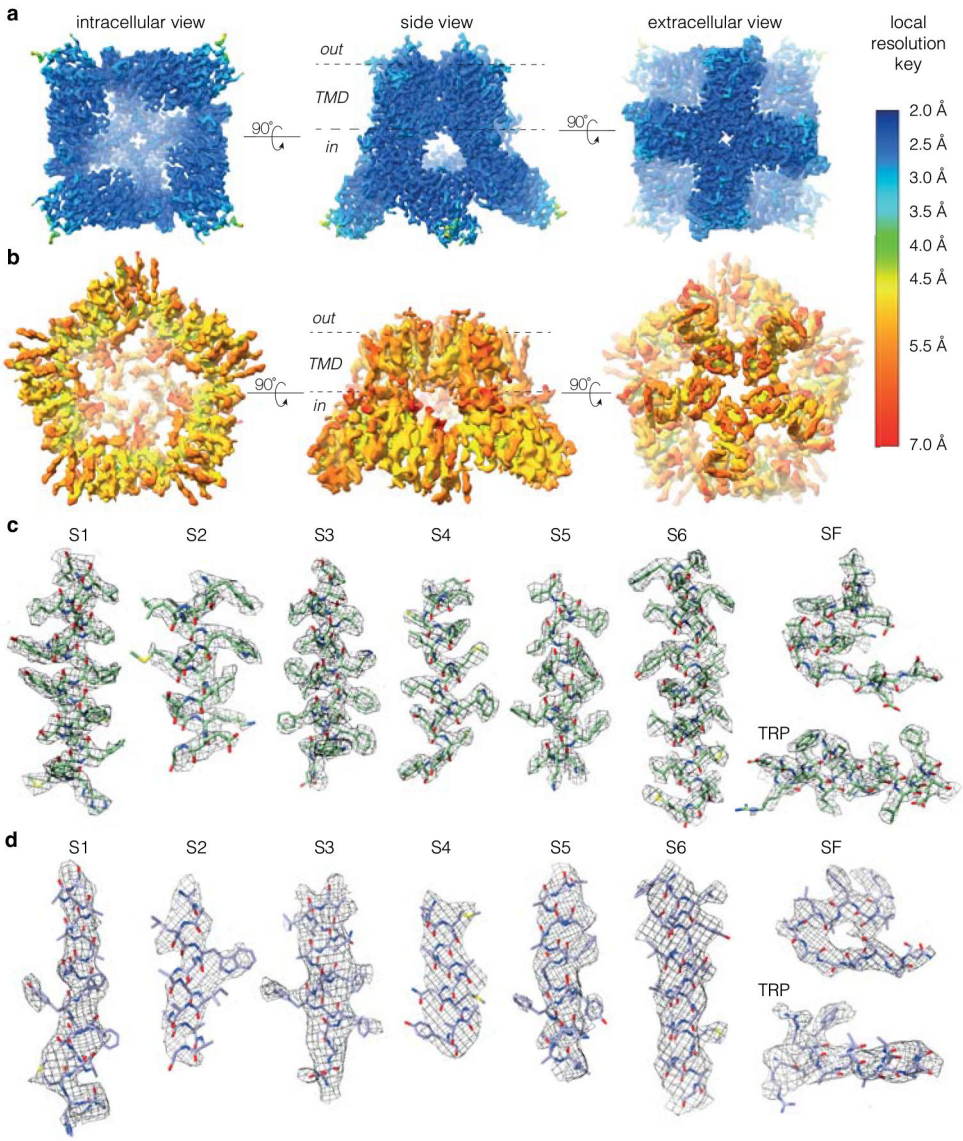

Extended Data Figure 6 |. Cryo-EM density maps of the TRPV3 tetramer and pentamer.

(a) and **(b)** Cryo-EM reconstructed maps of the TRPV3 tetramer (a) and pentamer (b), colored according to local resolution using a rainbow color scale. **(c)** and **(d)** Representative cryo-EM densities of the tetramer (contour level at 5.5 RMSD) (c) and pentamer (contour level at 4.16 RMSD) (d), at 2.55Å and 4.38Å resolution, respectively (the TMDs in the pentamer map are of ~5.0–5.5 Å resolution, see local resolution color scheme in (b))

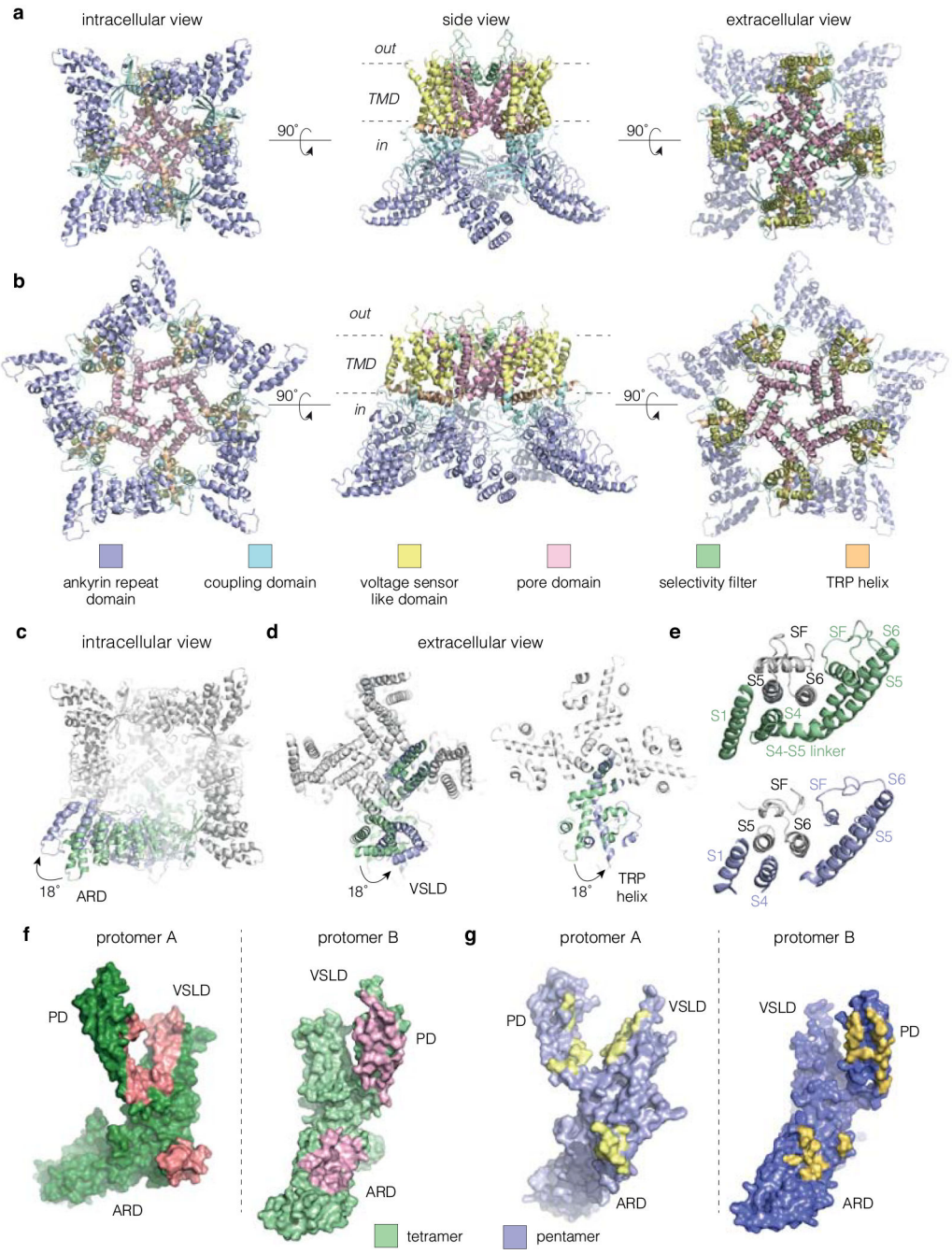

Extended Data Figure 7 |. Structural comparison of the TRPV3 tetramer and pentamer cryo-EM structures.

(**a**) and (**b**) TRPV3 tetramer (a) and pentamer (b) structures, colored according to domains: ARD in purple, VSLD in yellow, PD in pink, SF in green, TRP helix in wheat, coupling domain in light blue. (**c**) to (**e**) Superposition of a pentamer subunit (purple) onto the tetramer subunit (green), aligned with respect to the PD, indicating a hinge-motion in the pentamer monomer by 18°, as manifested by rotation of the ARD (**c**), VSLD, and TRP helix **(d)**. This hinge-motion enables preservation of the inter-subunit interactions of S5 with S1 and S4, and the SF-SF and S6-S6 interactions (e). Neighboring subunits in gray. Open

book graphics of the tetramer (**f**, green) and pentamer (**g**, purple) inter-subunit contact areas. Contact areas are colored in pink (in the tetramer) and yellow (in the pentamer).

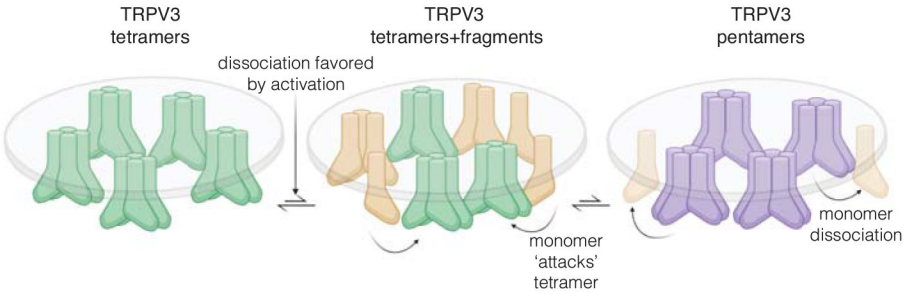

Extended Data Figure 8 |. Model of the reversible transition between the tetrameric and pentameric TRPV3 states.

TRPV3 tetramers may dissociate. Dissociation is favored by activation, due to destabilization of the inter-protomer interaction, notably the VSLD-PD domain-swap interface, by helix-intercalating molecules (*e.g.*, capsaicin or LPA in TRPV1, DPBA in TRPV3, temperature). Monomers may 'attack' and insert into tetramers to yield pentamers with an estimated ~2.4-fold enlarged pore diameter at the SF. Pentamers, lifetime of ~3 minutes, are however less stable than tetramers, due to more fragile VSLD-PD interfaces and shed subunits to regain the tetrameric state (figure created with BioRender).

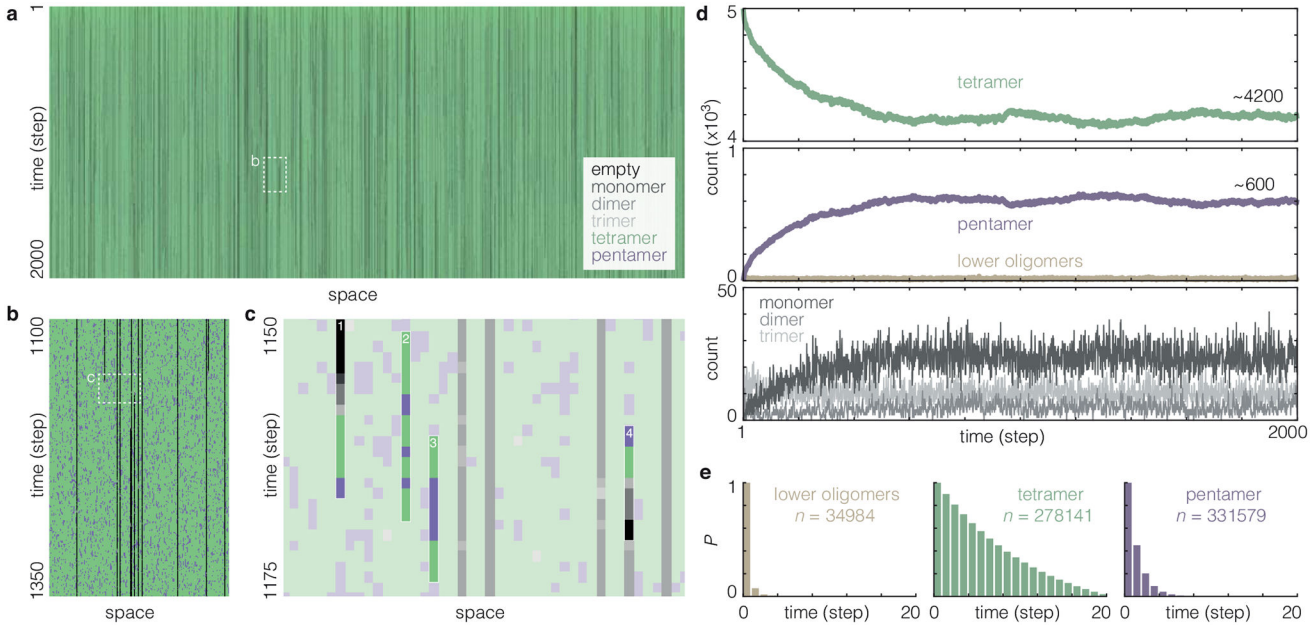

Extended Data Figure 9 |. Simulation of oligomeric state transitions.

(a) Visualization of simulated traces. Each column represents an independent space that can be either empty (0) or occupied by a molecule with a specific oligomeric state (1, 2, 3, 4 or 5). Total space: 5250. Total time step: 2000. Initial setup (time step = 1): 5000 out of 5250 spaces had a value of 4 (tetramers) and 250 out of the 5250 spaces had a value of 0 (empty). **(b)** and **(c)** Close-up views of the simulated traces in (a) as indicated by the dashed boxes. 1: Empty → monomer → dimer → trimer → tetramer → pentamer transition. 2: Transitions

between tetramer and pentamer states (with short pentamer dwell-times). 3: A long pentamer state event. 4: pentamer → tetramer → trimer → dimer → monomer → empty transition. **(d)** Time-evolution of oligomer counts. Top panel: Tetramers. Middle panel: Pentamers and lower oligomers (trimer, dimer, and monomer) aggregated. Bottom panel: Trimers, dimers and monomers. **(e)** Oligomer state dwell-times. Left to right: Lower oligomers (n = 34984), tetramer (n = 278141), and pentamer (n = 331579).

Extended Data Table 1 |

Cryo-EM data collection, refinement, and validation statistics. Cryo-EM data collection and structure refinement statistics of the TRPV3 tetramer (left) and pentamer (right).

	Tetramer (EMDB-40181) (PDB 8GKA)	**Pentamer (EMDB-40183) (PDB 8GKG)**
Data collection and processing		
Magnification	64,000X	64,000X
Voltage (kV)	300	300
Electron exposure (e^{-}/Å^2)	53.27	53.27
Defocus range (μm)	−0.8 to −2.5	−0.8 to −2.5
Pixel size (Å)	1.076	1.076
Symmetry imposed	C4	C5
Initial particle images (no.)	3,668,517	3,668,517
Final particle images (no.)	1,532,979	30,186
Map resolution (Å)	2.55	4.38
FSC threshold	0.143	0.143
Map resolution range (Å)	2.4 – 4.5	4.1 – 7.0
Refinement		
Initial model used (PDB code)	6UW4	6UW4
Model resolution (Å)	2.8	5.3
FSC threshold	0.5	0.5
Map sharpening *B* factor (Å^2)	−121.6	−179.3
Model composition		
Non-hydrogen atoms	21,812	17,160
Protein residues	2,500	2,700
Ligands	34	0
B factors (Å^2)		
Protein	44.5	159.5
Ligand	26.2	0
R.m.s. deviations		
Bond lengths (Å)	0.001	0.002
Bond angles (°)	0.385	0.541
Validation		
MolProbity score	1.60	2.00
Clashscore	7.21	5.72
Poor rotamers (%)	0.54	0.00

	Tetramer (EMDB-40181) (PDB 8GKA)	Pentamer (EMDB-40183) (PDB 8GKG)
Ramachandran plot		
Favored (%)	96.78	83.40
Allowed (%)	3.22	16.42
Disallowed (%)	0.00	0.19

Supplementary Material

Refer to Web version on PubMed Central for supplementary material.

Acknowledgments

We thank Alessio Accardi and Jeremy Dittman for important discussions. Negative-stain EM data were collected in the Electron Microscopy & Histology services of the Weill Cornell Medicine Microscopy & Image Analysis Core using a TEM purchased with funds from an NIH Shared Instrumentation Grant (S10RR027699) for Shared Resources. Cryo-EM data were collected at the Simons Electron Microscopy Center at the New York Structural Biology Center, with support from the Simons Foundation (SF349247). Work in the Scheuring laboratory is partly supported by grants from the National Institute of Health (NIH), National Center for Complementary and Integrative Health (NCCIH), DP1AT010874 (to SS), and National Institute of Neurological Disorders and Stroke (NINDS), R01NS110790 (to SS). Work in the Yuan laboratory is partly supported by NIH NINDS R01NS099341 (to PY). Work in the Nimigean laboratory is partly supported by NIH NIMGS R01 GM088352 (to CMN) and NIH NIMGS F32 GM145091 (to EDK). SL is an awardee of the Weizmann Institute of Science Women's Postdoctoral Career Development Award.

References

1. Peng G, Shi X & Kadowaki T Evolution of TRP channels inferred by their classification in diverse animal species. Mol. Phylogenet. Evol 84, 145–157 (2015). [PubMed: 24981559]
2. Himmel NJ & Cox DN Transient receptor potential channels: current perspectives on evolution. Proc. R. Soc. B Biol. Sci 287, 1–9 (2020).
3. Khalil M et al. Functional role of transient receptor potential channels in immune cells and epithelia. Front. Immunol 9, 1–7 (2018). [PubMed: 29403488]
4. Huffer KE, Aleksandrova AA, Jara-Oseguera A, Forrest LR & Swartz KJ Global alignment and assessment of trp channel transmembrane domain structures to explore functional mechanisms. Elife 9, 1–33 (2020).
5. Moran MM TRP Channels as Potential Drug Targets. Annu. Rev. Pharmacol. Toxicol 58, 309–330 (2018). [PubMed: 28945977]
6. Ferreira LGB & Faria RX TRPing on the pore phenomenon: what do we know about transient receptor potential ion channel-related pore dilation up to now? J. Bioenerg. Biomembr 48, 1–12 (2016). [PubMed: 26728159]
7. Zheng J & Ma L Structure and Function of the ThermoTRP Channel Pore. Curr. Top. Membr 74, 233–257 (2014). [PubMed: 25366239]
8. Liao M, Cao E, Julius D & Cheng Y Structure of the TRPV1 ion channel determined by electron cryo-microscopy. Nature 504, 107–112 (2013). [PubMed: 24305160]
9. Bai XC, Fernandez IS, McMullan G & Scheres SHW Ribosome structures to near-atomic resolution from thirty thousand cryo-EM particles. Elife 2013, 2–13 (2013).
10. Caterina MJ et al. The capsaicin receptor: A heat-activated ion channel in the pain pathway. Nature 389, 816–824 (1997). [PubMed: 9349813]
11. Kashio M & Tominaga M TRP channels in thermosensation. Curr. Opin. Neurobiol 75, 102591 (2022). [PubMed: 35728275]

12. van Goor MKC, Hoenderop JGJ & van der Wijst J TRP channels in calcium homeostasis: from hormonal control to structure-function relationship of TRPV5 and TRPV6. Biochim. Biophys. Acta - Mol. Cell Res 1864, 883–893 (2017). [PubMed: 27913205]
13. Pumroy RA et al. Molecular mechanism of TRPV2 channel modulation by cannabidiol. Elife 8, 1–17 (2019).
14. Xu H, Delling M, Jun JC & Clapham DE Oregano, thyme and clove-derived flavors and skin sensitizers activate specific TRP channels. Nat. Neurosci 9, 628–635 (2006). [PubMed: 16617338]
15. Deng Z et al. Cryo-EM and X-ray structures of TRPV4 reveal insight into ion permeation and gating mechanisms. Nat. Struct. Mol. Biol 25, 252–260 (2018). [PubMed: 29483651]
16. Deng Z et al. Gating of human TRPV3 in a lipid bilayer. Nat. Struct. Mol. Biol 27, 635–644 (2020). [PubMed: 32572252]
17. Nadezhdin KD et al. Structural mechanism of heat-induced opening of a temperature-sensitive TRP channel. Nat. Struct. Mol. Biol 28, (2021).
18. Zubcevic L et al. Conformational ensemble of the human TRPV3 ion channel. Nat. Commun 9, 1–12 (2018). [PubMed: 29317637]
19. Nilius B, Bíró T & Owsianik G TRPV3: Time to decipher a poorly understood family member! J. Physiol 592, 295–304 (2014). [PubMed: 23836684]
20. Bautista D & Julius D Fire in the hole: pore dilation of the capsaicin receptor TRPV1. Nat. Neurosci 11, 528–529 (2008). [PubMed: 18437189]
21. Chung MK, Güler AD & Caterina MJ TRPV1 shows dynamic ionic selectivity during agonist stimulation. Nat. Neurosci 11, 555–564 (2008). [PubMed: 18391945]
22. Zhang K, Julius D & Cheng Y Structural snapshots of TRPV1 reveal mechanism of polymodal functionality. Cell 184, 5138–5150.e12 (2021). [PubMed: 34496225]
23. Canul-Sánchez JA et al. Different agonists induce distinct single-channel conductance states in TRPV1 channels. J. Gen. Physiol 150, 1735–1746 (2018). [PubMed: 30409787]
24. Nieto-Posadas A et al. Lysophosphatidic acid directly activates TRPV1 through a C-terminal binding site. Nat. Chem. Biol 8, 78–85 (2012).
25. Chung MK, Güler AD & Caterina MJ Biphasic currents evoked by chemical or thermal activation of the heat-gated ion channel, TRPV3. J. Biol. Chem 280, 15928–15941 (2005). [PubMed: 15722340]
26. Chen J et al. Pore dilation occurs in TRPA1 but not in TRPM8 channels. Mol. Pain 5, 2–7 (2009). [PubMed: 19138413]
27. Banke TG, Chaplan SR & Wickenden AD Dynamic changes in the TRPA1 selectivity filter lead to progressive but reversible pore dilation. Am. J. Physiol. - Cell Physiol 298, 1457–1468 (2010).
28. Zubcevic L, Le S, Yang H & Lee SY Conformational plasticity in the selectivity filter of the TRPV2 ion channel. Nat. Struct. Mol. Biol 25, 405–415 (2018). [PubMed: 29728656]
29. Uchihashi T & Scheuring S Applications of high-speed atomic force microscopy to real-time visualization of dynamic biomolecular processes. Biochim. Biophys. Acta - Gen. Subj 1862, 229–240 (2018). [PubMed: 28716648]
30. Heath GR & Scheuring S Advances in high-speed atomic force microscopy (HS-AFM) reveal dynamics of transmembrane channels and transporters. Curr. Opin. Struct. Biol 57, 93–102 (2019). [PubMed: 30878714]
31. Misetic V, Reiners O, Krauss U & Jaeger K-E nanoDSF Thermal Unfolding Analysis of Proteins Without Tryptophan Residues. Thermal Unfolding, Appl. Note NT-PR-007 1–4 (2016).
32. Real-Hohn A, Groznica M, Löffler N, Blaas D & Kowalski H nanoDSF: In vitro Label-Free Method to Monitor Picornavirus Uncoating and Test Compounds Affecting Particle Stability. Front. Microbiol 11, 1–12 (2020). [PubMed: 32082274]
33. Grubisha O et al. Pharmacological profiling of the TRPV3 channel in recombinant and native assays. Br. J. Pharmacol 171, 2631–2644 (2014). [PubMed: 23848361]
34. Yu FH, Yarov-Yarovoy V, Gutman GA & Catterall WA Overview of molecular relationships in the voltage-gated ion channel superfamily. Pharmacol. Rev 57, 387–395 (2005). [PubMed: 16382097]
35. Nadezhdin KD et al. Extracellular cap domain is an essential component of the TRPV1 gating mechanism. Nat. Commun 12, 4–11 (2021). [PubMed: 33397975]

36. Singh AK, Saotome K & Sobolevsky AI Swapping of transmembrane domains in the epithelial calcium channel TRPV6. Sci. Rep 7, 1–10 (2017). [PubMed: 28127051]
37. Yelshanskaya MV & Sobolevsky AI Ligand-Binding Sites in Vanilloid-Subtype TRP Channels. Front. Pharmacol 13, 1–21 (2022).
38. Singh AK, McGoldrick LL & Sobolevsky AI Structure and gating mechanism of the transient receptor potential channel TRPV3. Nat. Struct. Mol. Biol 25, 805–813 (2018). [PubMed: 30127359]
39. Zubcevic L, Borschel WF, Hsu AL, Borgnia MJ & Lee SY Regulatory switch at the cytoplasmic interface controls trpv channel gating. Elife 8, 1–24 (2019).
40. Ni C et al. A novel mutation in TRPV3 gene causes atypical familial Olmsted syndrome. Sci. Rep 6, 1–10 (2016). [PubMed: 28442746]
41. Duchatelet S et al. A new TRPV3 missense mutation in a patient with Olmsted syndrome and erythromelalgia. JAMA Dermatology 150, 303–306 (2014). [PubMed: 24452206]
42. Jiang Y et al. Membrane-mediated protein interactions drive membrane protein organization. Nat. Commun 13, 1–14 (2022). [PubMed: 34983933]
43. Hazan A, Kumar R, Matzner H & Priel A The pain receptor TRPV1 displays agonist-dependent activation stoichiometry. Sci. Rep 5, 1–13 (2015).
44. Sente A et al. Differential assembly diversifies GABAA receptor structures and signalling. Nature 604, 190–194 (2022). [PubMed: 35355020]
45. Noviello CM, Kreye J, Teng J, Prüss H & Hibbs RE Structural mechanisms of GABAA receptor autoimmune encephalitis. Cell 185, 2469–2477 (2022). [PubMed: 35803245]
46. Cheng W, Yang F, Takanishi CL & Zheng J Thermosensitive TRPV channel subunits coassemble into heteromeric channels with intermediate conductance and gating properties. J. Gen. Physiol 129, 191–207 (2007). [PubMed: 17325193]
47. Bleakman D, Brorοson JR & Miller RJ The effects of capsaicin on voltage-gated calcium currents and calcium signals in cultured dorsal root ganglion cells. Br. J. Pharmacol 101, 423–431 (1990). [PubMed: 1701680]
48. Evans AR, Nicol GD & Vasko MR Differential regulation of evoked peptide release by voltage-sensitive calcium channels in rat sensory neurons. Brain Res 712, 265–273 (1996). [PubMed: 8814901]
49. Jancso G Pathobiological reactions of C-fibre primary sensory neurones to peripheral nerve injury. Exp. Physiol 77, 405–431 (1992). [PubMed: 1321641]
50. Goehring A et al. Screening and large-scale expression of membrane proteins in mammalian cells for structural studies. Nat. Protoc 9, 2574–2585 (2014). [PubMed: 25299155]
51. Sanganna Gari RR et al. Correlation of membrane protein conformational and functional dynamics. Nat. Commun 12, 1–11 (2021). [PubMed: 33397941]
52. Heath GR et al. Localization atomic force microscopy. Nature 594, 385–390 (2021). [PubMed: 34135520]
53. Matin TR, Heath GR, Scheuring S & Boudker O Millisecond dynamics of an unlabeled amino acid transporter. Nat. Commun 11, 1–11 (2020). [PubMed: 31911652]
54. Rangl M, Schmandt N, Perozo E & Scheuring S Real Time Dynamics of Gating-Related Conformational Changes in CorA. Elife 8, e47322 (2019). [PubMed: 31774394]
55. Lin YC et al. Force-induced conformational changes in PIEZO1. Nature 573, 230–234 (2019). [PubMed: 31435018]
56. Ruan Y et al. Structural titration of receptor ion channel GLIC gating by HS-AFM. Proc. Natl. Acad. Sci 115, 10333–10338 (2018). [PubMed: 30181288]
57. Ruan Y et al. Direct visualization of glutamate transporter elevator mechanism by high-speed AFM. Proc. Natl. Acad. Sci 114, 1584–1588 (2017). [PubMed: 28137870]
58. Schneider CA, Rasband WS & Eliceiri KW NIH Image to ImageJ: 25 years of image analysis. Nat. Methods 9, 671–675 (2012). [PubMed: 22930834]
59. Suloway C et al. Automated molecular microscopy: The new Leginon system. J. Struct. Biol 151, 41–60 (2005). [PubMed: 15890530]

60. Punjani A, Rubinstein JL, Fleet DJ & Brubaker MA CryoSPARC: Algorithms for rapid unsupervised cryo-EM structure determination. Nat. Methods 14, 290–296 (2017). [PubMed: 28165473]
61. Bepler T et al. Positive-unlabeled convolutional neural networks for particle picking in cryo-electron micrographs. Nat. Methods 16, 1153–1160 (2019). [PubMed: 31591578]
62. Chen S et al. High-resolution noise substitution to measure overfitting and validate resolution in 3D structure determination by single particle electron cryomicroscopy. Ultramicroscopy 135, 24–35 (2013). [PubMed: 23872039]
63. Paknejad N, Sapuru V & Hite RK Structural titration reveals Ca2+-dependent conformational landscape of the IP3 receptor. bioRxiv 2022.12.29.522241 (2022).
64. Kimanius D, Dong L, Sharov G, Nakane T & Scheres SHW New tools for automated cryo-EM single-particle analysis in RELION-4.0. Biochem. J 478, 4169–4185 (2021). [PubMed: 34783343]
65. Terwilliger TC, Sobolev OV, Afonine PV, Adams PD & Read RJ Density modification of cryo-EM maps. Acta Crystallogr. Sect. D Struct. Biol 76, 912–925 (2020). [PubMed: 33021493]
66. Pettersen EF et al. UCSF Chimera--a visualization system for exploratory research and analysis. J. Comput. Chem 25, 1605–1612 (2004). [PubMed: 15264254]
67. Zwart PH et al. Automated structure solution with the PHENIX suite. Methods Mol. Biol 426, 419–435 (2008). [PubMed: 18542881]
68. Emsley P & Cowtan K Coot: Model-building tools for molecular graphics. Acta Crystallogr. Sect. D Biol. Crystallogr 60, 2126–2132 (2004). [PubMed: 15572765]
69. Chen VB et al. MolProbity: All-atom structure validation for macromolecular crystallography. Acta Crystallogr. Sect. D Biol. Crystallogr 66, 12–21 (2010). [PubMed: 20057044]
70. Afonine PV et al. Real-space refinement in PHENIX for cryo-EM and crystallography. Acta Crystallogr. Sect. D Struct. Biol 74, 531–544 (2018). [PubMed: 29872004]

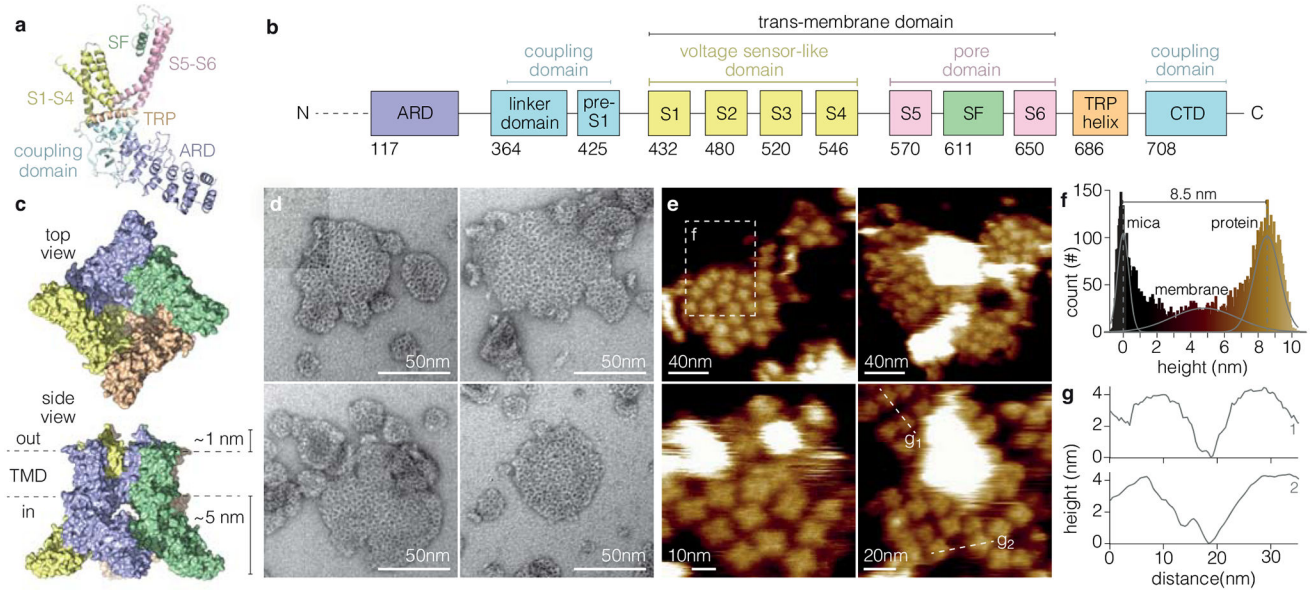

Figure 1 |. Membrane reconstitution of TRPV3.

(**a**) TRPV3 subunit architecture, with ankyrin repeat domain (ARD, purple), linker domain and pre-S1 (blue), voltage sensor like domain (VSLD, S1-S4, yellow), pore domain (S5-SF-S6, pink-green-pink), TRP-helix (wheat), and C-terminal domain (CTD, blue). (**b**) Sequence representation, color-coded as in (a). (**c**) Intracellular (top) and side (bottom) views of the human TRPV3 tetramer structure (PDB 6uw4), the four subunits are color coded. The VSLD is domain-swapped with respect to the PD, *e.g.*, the VSLD of the purple subunit interacts with the pore domain of the yellow subunit. (**d**) Representative negative-stain EM images of TRPV3 reconstitutions in yeast polar lipid and POPC:DOPS:cholesterol (8:1:1, w:w:w) membranes. Similar reconstitutions and EM images were reproduced >20 times. (**e**) Overview HS-AFM video frames of TRPV3 reconstitutions. (**f**) Height distribution analysis of dashed outline in (e, top left), colored according to the height false-color scale. (**g**) Cross-section analysis along dashed lines in (e, bottom right).

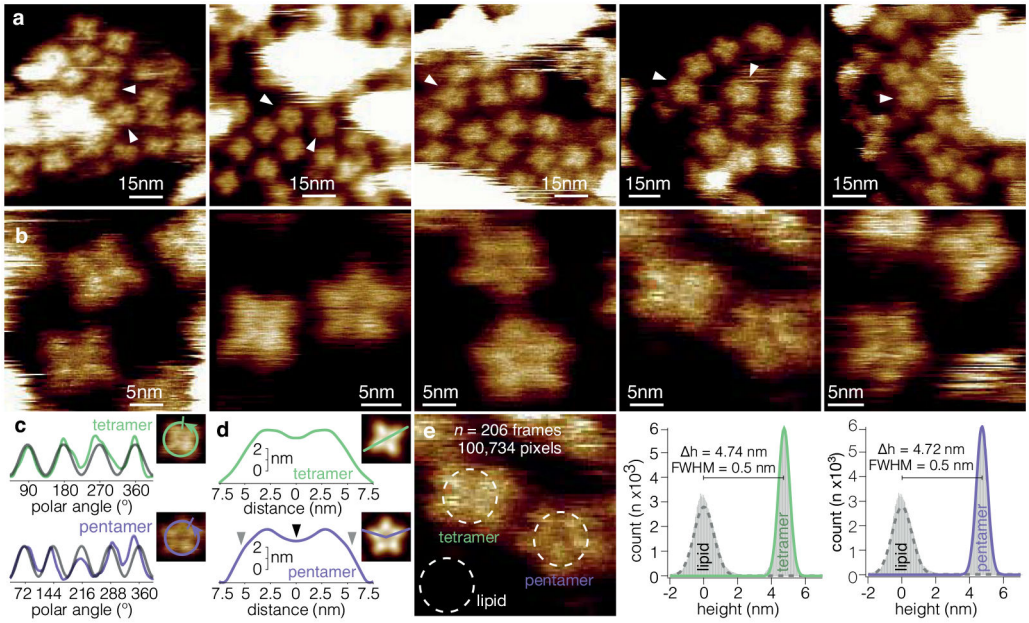

Figure 2 |. TRPV3 pentamers coexist with canonical TRPV3 tetramers in membranes.

(**a**) Medium-resolution HS-AFM videos frames (Supplementary Videos 5–9) of TRPV3 in membranes revealed several channels with pentameric oligomeric state (arrowheads). (**b**) High-resolution HS-AFM video frames (Supplementary Videos 10–15) of tetrameric and pentameric TRPV3 channels. (**c**) Radial profiles of TRPV3 tetramer (green) and pentamer (purple) individual molecules (from (b), panel 2). The black lines represent sine fits with 90° and 72° peak periodicity, respectively. (**d**) Height profiles of tetramer (green) and pentamer (purple) correlation averages (from (b), panel 2) along green and purple lines in the insets, respectively. (**e**) Protrusion height analysis: Histograms of height distributions of TRPV3 tetramer (middle, green) and pentamer (right, purple) relative to the lipid bilayer. Left: Dashed outlines of central regions of tetramer, pentamer and lipid bilayer area (8.5nm diameter) from which the height values were extracted (from (b), panel 4) from 100,734 pixels (489 pixels in 206 frames).

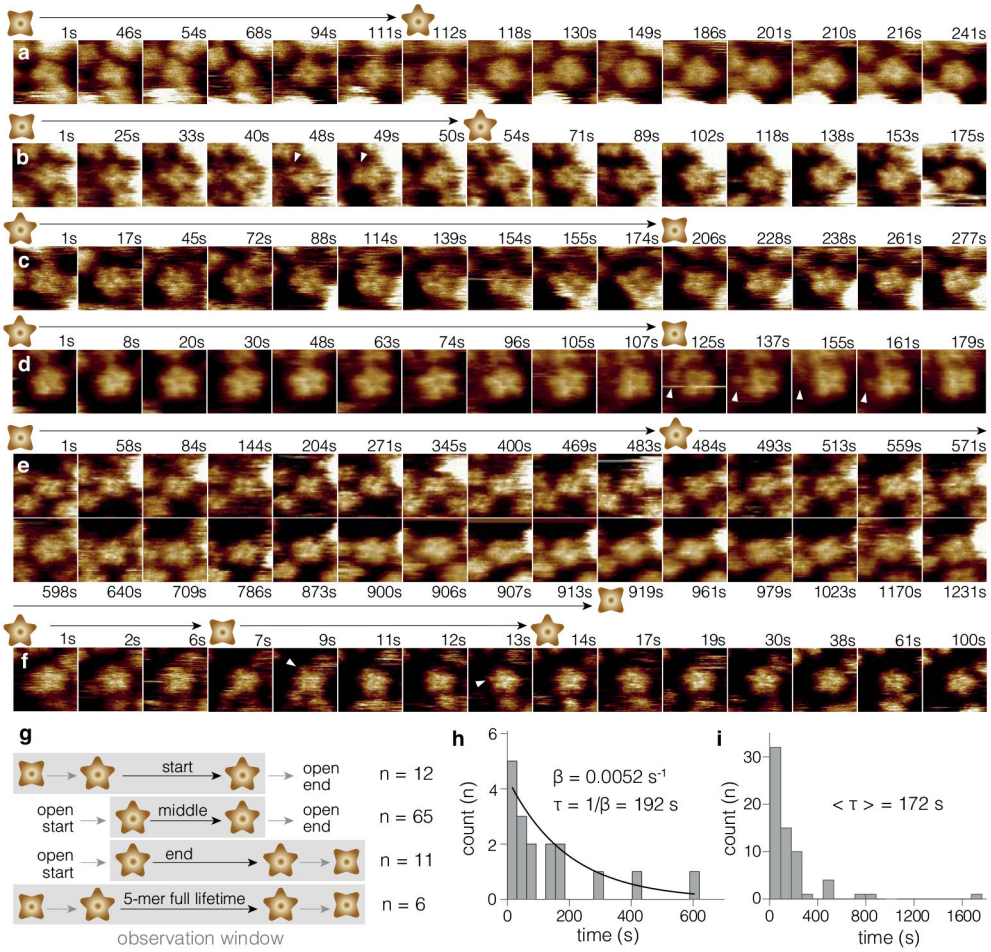

Figure 3 |. TRPV3 tetramer–pentamer and pentamer–tetramer transitions, and observations of complete reversibility between the tetramer and pentamer state.

(**a**) and (**b**) TRPV3 tetramer–pentamer transitions. (**c**) and (**d**) TRPV3 pentamer–tetramer transitions. (**e**) TRPV3 tetramer–pentamer–tetramer transition. (**f**) TRPV3 pentamer–tetramer–pentamer transition. White arrowheads indicate monomers 'attacking' and inserting tetramers and dissociating from pentamers, respectively. (**g**) Number and type of observed (grey areas indicate observation window) transitions. From top to bottom: Pentamer state observations that were open ended, pentamer observations that had no beginning nor end, pentamers that were observed transforming into tetramers, and observations that comprised the beginning and the end, *i.e.*, full lifetime, of the pentamer state (complete tetramer–pentamer–tetramer transitions). (**h**) Dwell-times of pentamer states that were observed transforming into tetramers ($n = 17$). The histogram was fit with an exponential decay, $\tau = 192$ s, adj. $R^2 = 0.77$. (**i**) Dwell-times of pentamer states that had no beginning nor end ($n = 65$). Average dwell-time $< \tau > = 172$ s.

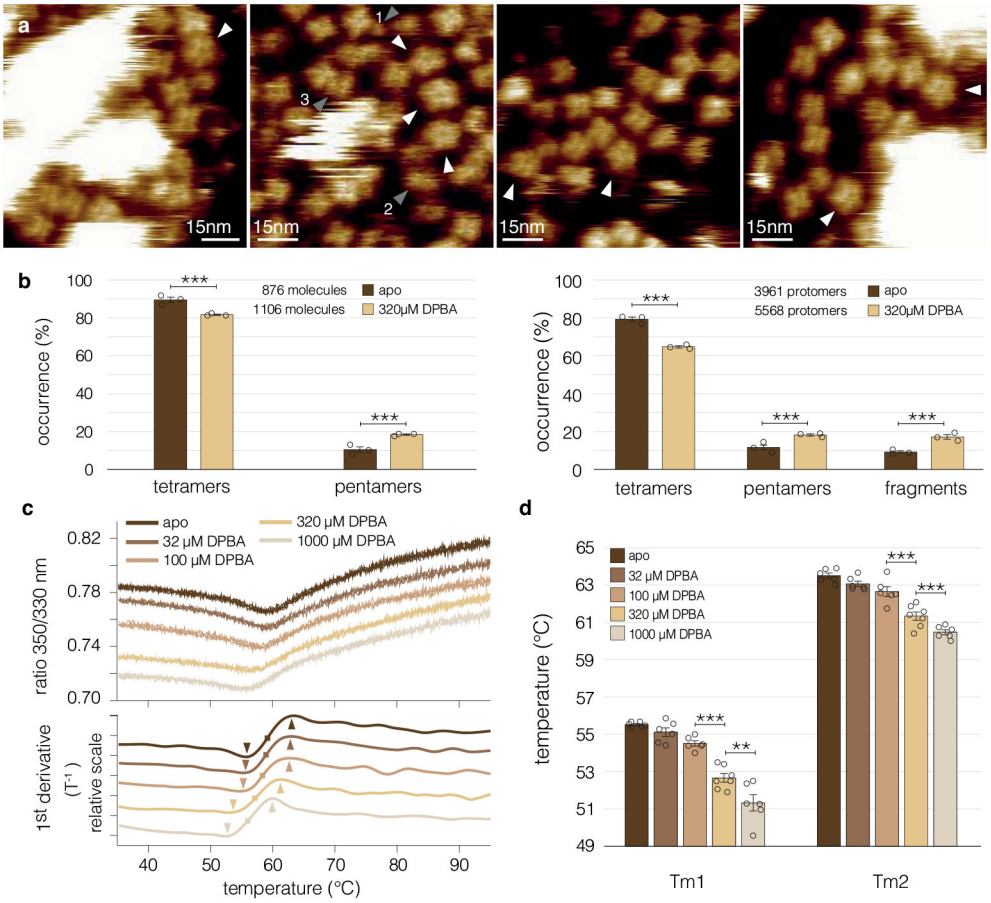

Figure 4 |. DPBA leads to an increase of TRPV3 pentamers.

(**a**) HS-AFM videos frames of membrane-embedded TRPV3 in the presence of 320 μM DPBA. Among many tetramers, TRPV3 pentamers (white arrowheads) and fragments (grey arrowheads; 1-monomer, 2-dimer, 3-trimer) were observed. (**b)** Statistics of tetramer and pentamer populations (left), and tetramer, pentamer, and fragment populations (right), in the absence (dark brown) and presence (light brown) of 320 μM DPBA. Data are presented as mean values +/− SEM of the population percentages derived from $n = 3$ biologically independent samples (circles). Statistical significance was assessed with the one-tailed two proportion Z-test, yielding in all cases absolute Z-values > 4.9, corresponding to p-values < 0.0001. (**c**) Thermal denaturation profiles of TRPV3 (raw data (top) and 1st derivative (bottom; squares indicate $f' = 0$ (traces are vertically shifted for clarity) Tm1 (downwards arrowheads) and Tm2 (upwards arrowheads)) in the absence (black) and presence of 32 μM ($n = 6$ biologically independent experiments), 100 μM ($n = 6$), 320 μM ($n = 7$), and 1000 μM DPBA ($n = 6$), colored with increasingly lighter shades of brown, indicate a (**d**) significant reduction of Tm1 and Tm2 following the addition of 320 μM and 1000 μM DPBA. Tm values are presented as mean values +/− SEM of the Tm results (circles) obtained from $n = 6$ or 7 biologically independent experiments. Statistical significance was assessed with the one-tailed Welch's T-test, yielding a significant reduction (99% confidence level) in both Tm1 and Tm2 following addition of 320 μM DPBA (p-value = 0.000038 and 0.0019, respectively), and a further significant reduction in Tm1 and Tm2 following addition of 1000

μM DPBA (p-value = 0.015 (95% confidence level) and 0.0043 (99% confidence level). **p-value <0.025; ***p-value <0.005.

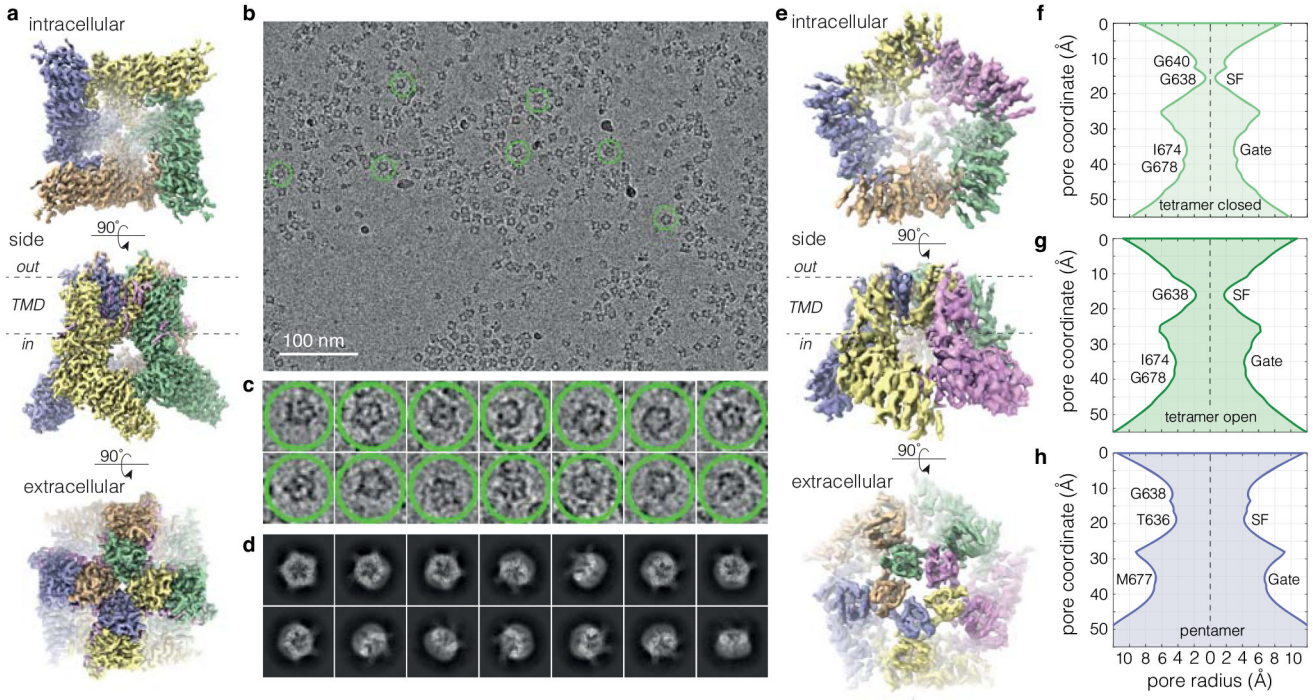

Figure 5 |. Cryo-EM structures of the TRPV3 channel tetramer and pentamer.

(**a**) Cryo-EM map of the TRPV3 tetramer, determined to 2.6 Å resolution. The four protein subunits are colored in wheat, purple, yellow, and green, and the lipid densities are colored in pink. (**b**) A representative cryo-EM micrograph (out of 10,118 similar micrographs), showing that a small percentage of molecules in the raw data have (**c**) clear pentameric architecture (only pentamer top views are identifiable to the eye). (**d**) Representative 2D class averages of the TRPV3 pentamer in different orientations. (**e**) Cryo-EM map of the TRPV3 pentamer, determined to 4.4 Å resolution. The five protein subunits are colored in wheat, purple, yellow, pink, and green. (**f**) Pore profile of the tetramer structure, (**g**) pore profile of a previously determined tetramer open conformation TRPV3 mutant (K169A) (PDB 6UW6)[16], and (**h**) pore profile of the TRPV3 pentamer. All pore profiles were calculated by considering only the backbone.